The Astrophysical Journal, 813:120 (16pp), 2015 November 10 doi:10.1088/0004-637X/813/2/120


# HETEROGENEITY IN $^{12}CO/^{13}CO$ ABUNDANCE RATIOS TOWARD SOLAR-TYPE YOUNG STELLAR OBJECTS

Rachel L. Smith[1,2], Klaus M. Pontoppidan[3], Edward D. Young[4], and Mark R. Morris[5]
[1] North Carolina Museum of Natural Sciences, 121 West Jones Street, Raleigh, NC 27603, USA; rachel.smith@naturalsciences.org
[2] Department of Physics and Astronomy, Appalachian State University, 525 Rivers Street, Boone, NC 28608-2106, USA; smithrl2@appstate.edu
[3] Space Telescope Science Institute, 3700 San Martin Drive, Baltimore, MD 21218, USA
[4] Department of Earth, Planetary, and Space Sciences, University of California Los Angeles, 595 Charles E. Young Drive East, Geology Building, Los Angeles, CA 90095-1567, USA
[5] Division of Astronomy and Astrophysics, Department of Physics and Astronomy, University of California, Los Angeles, CA 90095-1547, USA
*Received 2012 May 13; accepted 2015 August 30; published 2015 November 5*

## ABSTRACT

This study reports an unusual heterogeneity in $[^{12}C^{16}O]/[^{13}C^{16}O]$ abundance ratios of carbon monoxide observed in the gas phase toward seven ∼solar-mass young stellar objects (YSOs) and three dense foreground clouds in the nearby star-forming regions, Ophiuchus, Corona Australis, Orion, and Vela, and an isolated core, L43. Robust isotope ratios were derived using infrared absorption spectroscopy of the 4.7 $\mu$m fundamental and 2.3 $\mu$m overtone rovibrational bands of CO at very high spectral resolution ($\lambda/\Delta\lambda \approx 95{,}000$), observed with the Cryogenic Infrared Echelle Spectrograph (CRIRES) on the Very Large Telescope. We find $[^{12}C^{16}O]/[^{13}C^{16}O]$ values ranging from ∼85 to 165, significantly higher than those of the local interstellar medium (ISM) (∼65–69). These observations are evidence for isotopic heterogeneity in carbon reservoirs in solar-type YSO environments, and encourage the need for refined galactic chemical evolution models to explain the $^{12}C/^{13}C$ discrepancy between the solar system and local ISM. The oxygen isotope ratios are consistent with isotopologue-specific photodissociation by CO self-shielding toward the disks, VV CrA N and HL Tau, further substantiating models predicting CO self-shielding on disk surfaces. However, we find that CO self-shielding is an unlikely general explanation for the high $[^{12}C^{16}O]/[^{13}C^{16}O]$ ratios observed in this study. Comparison of the solid CO against gas-phase $[^{12}C^{16}O]/[^{13}C^{16}O]$ suggests that interactions between CO ice and gas reservoirs need to be further investigated as at least a partial explanation for the unusually high $[^{12}C^{16}O]/[^{13}C^{16}O]$ observed.

*Key words:* astrochemistry – infrared: stars – molecular processes – protoplanetary disks – stars: protostars – stars: solar-type

*Supporting material:* machine-readable tables

## 1. INTRODUCTION

Observations of carbon monoxide (CO) provide a robust window into circumstellar chemistry. Due to the large percentage of carbon (∼15%–30%) and oxygen (∼10%) tied up in CO in the early stages of young stellar object (YSO) formation (Dickman 1978), CO is a valuable tracer of chemical inheritance from the envelope to the disk in solar-type YSOs. The use of high-resolution spectroscopy to observe CO at infrared wavelengths enables high-precision investigations of isotope fractionation in both oxygen and carbon toward YSOs in embedded and disk-phase evolutionary stages, and is consequently an important tool for connecting the solar system to currently forming protoplanetary systems. Examples include observational studies toward diffuse clouds and inferring isotopologue-specific photodissociation by CO self-shielding as a potentially important mechanism of carbon isotope fractionation in CO in the interstellar medium (ISM; Bally & Langer 1982; Sheffer et al. 2002). Furthermore, high-resolution near-infrared observations of the CO rovibrational band toward protoplanetary disks (Brittain et al. 2005; Smith et al. 2009) and protostellar envelopes have recently revealed signatures in CO isotopologue ratios that are consistent with CO self-shielding, with precision sufficiently high for comparison to meteoritic data (Smith et al. 2009).

Observations of isotope ratios toward YSOs, and where possible, their parent clouds, are valuable for assessing theorized similarities between circumstellar envelopes, disks, and dense clouds that are local to their origin. This is important not only for evaluating predictions of galactic chemical evolution (GCE) models that are constrained by solar system abundances, but also for characterizing the range of carbon isotope ratios toward YSOs varying with evolutionary stage, and establishing accurate astrochemical constraints on protoplanetary environments. Observational studies can help demonstrate whether there are significant isotopic differences or trends between diffuse clouds, dense molecular clouds, and YSOs. These in turn help construct explanations for apparent chemical anomalies such as the $^{12}C/^{13}C$ solar system-ISM discrepancy and solar system oxygen isotope anomaly.

This paper focuses on the carbon isotopic systems in YSOs as traced by high-resolution observations of CO isotopologues, with additional mention of significant findings in oxygen isotopes. Current measurements of the $^{12}C/^{13}C$ ratio for the solar system are ∼86–89, derived from photospheric models applied to the solar CO spectrum (Scott et al. 2006), and bulk solar system materials (Rosman & Taylor 1998; Wilson 1999; Coplen et al. 2002; Clayton & Nittler 2004; Young et al. 2011). Values of $^{12}C/^{13}C$ for the solar system have been consistently higher than those of ∼62–69 observed toward the local ISM, measured using millimeter to submillimeter rotational transitions of various carbon-bearing molecules, CO, CN, $CH^+$, and $H_2CO$ (Langer & Penzias 1993; Wilson 1999; Casassus et al. 2005; Milam et al. 2005). The apparent discrepancy in $^{12}C/^{13}C$ between the solar system and the ISM has been attributed to

**Table 1**
Summary of Observed Targets

| Target | Region[a] | Distance (pc) | Comments[a] |
|---|---|---|---|
| DoAr24E S, N | Oph | 125 | Stage II/IR companion |
| IRS 43 | Oph | 125 | Stage I |
| IRS 51 | Oph | 125 | Extincted stage II |
| IRS 63[b] | Oph | 125 | Stage I |
| RNO 91 | L43 | 125 | Stage I |
| VV CrA N, S | CrA | 130 | Stage II/IR companion |
| HL Tau | Tau | 140 | Stage I |
| Reipurth 50 | Ori | 470 | Stage I/FU Ori |
| LLN 19 | Vel | 700 | Stage I |

**Notes.**
[a] The evolutionary stage refers to the system proposed by Robitaille et al. (2006). The two targets with N/S components are 1″–2″ binaries, for which the secondary is a highly extincted "infrared companion" (Koresko et al. 1997).
[b] IRS 63 may have formed from an isolated core (Ridge et al. 2006).

GCE leading to the enrichment of $^{13}$C relative to $^{12}$C over the ∼4.6 Gyr lifetime of the solar system (e.g., Prantzos et al. 1996; Milam et al. 2005). An important property of GCE models is the assumption that the solar system records the chemical state of the molecular cloud material ∼4.6 Gyr ago. That is, the assumption that the solar nebula was isotopically representative of its parent cloud at its Galactic radius at the time of formation should also hold for present-day solar-type YSOs.

The challenge for observational comparisons of solar system isotope ratios in general is the need for high precision in molecular abundance measurements. While techniques using strong rotational lines in the millimeter/submillimeter range often involve model-dependent comparisons between optically thick and thin lines, high-resolution infrared spectrographs have enabled significant breakthroughs in observations of nearby YSOs. Infrared absorption spectroscopy of optically thin CO lines allows for precise column density measurements along pencil-beam lines of sight, enabling the derivation of precise column densities and isotope ratios from the line profiles of as many as four currently observable CO isotopologues ($^{12}C^{16}O$, $^{13}C^{16}O$, $^{12}C^{18}O$, $^{12}C^{17}O$). Robust isotope ratios so derived can be compared with statistical significance to submillimeter ISM values, solar abundances, and meteoritic oxygen. A high degree of precision (within 10%) on the absolute values of the column densities has been demonstrated for the four most common CO isotopologues (Smith et al. 2009). The study reported here builds on this work.

Our targets span a range in $^{12}C^{16}O$ ("CO" may also designate this most common isotopologue) ice optical depth from nearly saturated to undetected, providing an opportunity to investigate a potential observational connection between the CO ice and gas reservoirs by comparing the gas-phase $[^{12}C^{16}O]/[^{13}C^{16}O]$ to the $^{12}C^{16}O$ ice column along a single line of sight. Since solids tend to concentrate the heavy isotope relative ice–gas partitioning may lead to a paucity of $^{13}$C (or excess of $^{12}$C) in the gas phase, with the opposite signature sequestered in the ice.

## 2. OBSERVATIONS

Data for all targets were obtained as part of a European Southern Observatory Large Program (Pontoppidan et al. 2011b) to observe ∼100 YSOs and protoplanetary disks with the Cryogenic Infrared Echelle Spectrograph (CRIRES) at the Very Large Telescope (VLT) in Chile. The CRIRES instrument is an adaptive optics (AO)-assisted spectrometer that operates at very high spectral resolving power ($\lambda/\Delta\lambda \approx 95{,}000$).

### 2.1. Strategy

Targets tracing high column densities of molecular gas were selected based on evidence of deep CO absorption lines at 4.7 $\mu$m in spectra obtained with VLT-ISAAC (Pontoppidan et al. 2003) and Keck-NIRSPEC (e.g., Boogert et al. 2002b).

**Table 2**
Summary of Observed Targets

| Target | R.A. (J2000) | Decl. (J2000) | Spectral Range ($\mu$m) | Obs. Date (UT) |
|---|---|---|---|---|
| DoAr24E S, N[a] | 16 26 23.36 | −24 20 59.8 | 4.644 – 4.768 | 2007 Sep 02 |
| | | | 2.338 – 2.396 | 2010 Mar 18 |
| IRS 43 | 16 27 26.94 | −24 40 50.8 | 4.645 – 4.900 | 2008 Aug 05 |
| | | | 2.338 – 2.396 | 2008 Aug 04 |
| IRS 51 | 16 27 39.83 | −24 43 15.1 | 4.645 – 4.768 | 2008 Aug 02 |
| | | | 2.338 – 2.391 | 2008 Aug 03 |
| IRS 63[a] | 16 31 35.65 | −24 01 29.3 | 4.645 – 4.978 | 2007 Apr 25 |
| | | | 2.338 – 2.396 | 2008 Aug 07 |
| RNO 91 | 16 34 29.28 | −15 47 01.5 | 4.645 – 4.855 | 2010 Mar 18 |
| | | | 2.338 – 2.396 | 2010 Apr 08 |
| VV CrA N, S | 19 03 06.74 | −37 12 49.7 | 4.701 – 4.815 | 2007 Aug 31 |
| | | | 2.338 – 2.396 | 2007 Aug 31 |
| HL Tau | 04 31 38.44 | 18 13 57.7 | 4.643 – 4.853 | 2010 Jan 30 |
| | | | 2.337 – 2.396 | 2010 Jan 28 |
| Reipurth 50 | 05 40 27.70 | −07 27 28.0 | 4.645 – 4.901 | 2007 Oct 11 |
| | | | 2.338 – 2.396 | 2007 Oct 17 |
| LLN 19 | 08 48 48.00 | −43 32 25.0 | 4.644 – 4.867 | 2007 Apr 25 |
| | | | 2.253 – 2.355 | 2007 Apr 25 |

**Note.**
[a] The non-coevality of these observations may contribute some level of uncertainty to the derived isotopic abundances, as discussed in the text.
(This table is available in machine-readable form.)

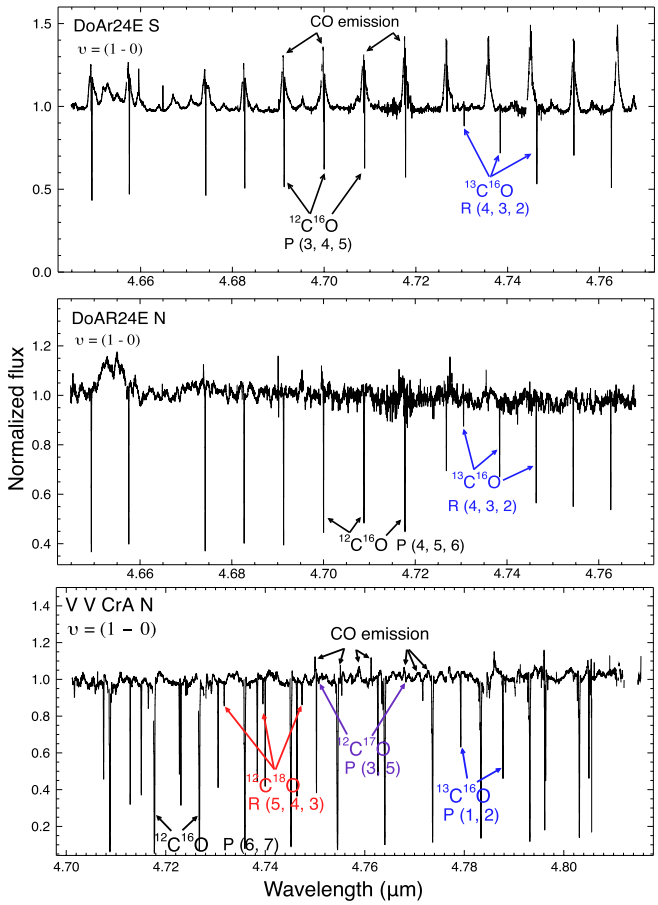


**Figure 1.** Infrared absorption spectra of the CO fundamental rovibrational band toward the DoAr24E N, S binary and the disk VV CrA N, which have weak $^{12}C^{16}O$ ice optical depth upper limits (Table 7). Spectra for DoAr24E N, S show few CO absorption lines, while VV CrA N shows a rich CO forest of narrow rovibrational absorption lines. Sample lines are marked. The low-level emission from hot CO gas toward DoAr24 S and VV CrA N is possibly representative of inner disk disk material. The weak emission line at ∼4.65 $\mu$m for DoAR24E N is HI Pfund $\beta$.

Selected targets were observed by CRIRES in the CO $\upsilon$ = (2–0) first-overtone, (*K*-) band at 2.3 $\mu$m and the $\upsilon$ = (1–0) fundamental (*M*-) band at 4.7 $\mu$m. Because the overtone transitions are weaker than those of the fundamental band by a factor of ∼100, the former are typically optically thin for $^{12}C^{16}O$, thereby enabling the precise measurement of column densities for this molecule. The spectra of the fundamental rovibrational bands were obtained using the 0.″2 slit, resulting in a resolving power of $R = \lambda/\Delta\lambda \approx 95{,}000$ (corresponding to 3.2 km s$^{-1}$). Several settings in the fundamental band were obtained for all targets in order to probe a range of rotational levels for $^{13}C^{16}O$, $^{12}C^{18}O$, and $^{12}C^{17}O$, spanning $J = 0$ to at least $J = 9$. Observations were timed such that the Doppler shifts of the targets relative to the Earth's atmosphere were at least 20 km s$^{-1}$, due to a combination of the intrinsic target velocity and reflex motion of the Earth. As a consequence, telluric CO lines are typically not affecting the absorption lines of the targets.

Table 1 summarizes the region, distance, and evolutionary stage of the observed targets, listed in order of increasing distance from the local solar neighborhood ($R_{GC} \sim 8$ kpc). Specific observing parameters are listed in Table 2. Selected targets probe a range of circumstellar environments as noted. Because the lines of sight traced by infrared absorption may pass through the upper layers of an inclined disk as well as through envelope material and a foreground molecular cloud unrelated to the YSO, some portion of each of these environments may be represented in the integrated spectra, depending on the target. For instance, near-infrared absorption spectra observed toward the extincted protoplanetary disk, IRS 51, will be an integrated sight line consisting mostly of the foreground Ophiuchus ridge and a relatively small contribution of the protoplanetary disk. This geometry has been predicted by interferometric observations (van Kempen et al. 2009) and is supported by our observations that reveal cold-only gas lines.

### 2.2. Data Reduction

The CRIRES spectra were reduced using standard procedures for infrared echelle spectroscopy, including flat-field correction, adjustments to account for detector nonlinearity, and linearization of the spectral traces in dispersion- and cross-dispersion directions. The spectra were optimally extracted, wavelength-calibrated using the telluric absorption lines referenced to an atmospheric model spectrum, and transformed to the local standard-of-rest frame. Relative flux calibration was carried out by dividing the targets by observations of early-type telluric standards observed immediately surrounding observations of the science target at the same airmass. The division was optimized by modifying the telluric spectra to account for any difference in grating angle, airmass, and spectral resolving power. To aid in the measurement of any intrinsic line broadening, the resolving powers for each science spectrum were measured from telluric spectra to within an accuracy of ∼0.1 km s$^{-1}$, by fitting the "Reference Forward Model" (RFM,[6] see also Section 3.2). Further details on CRIRES data processing are described in Pontoppidan et al. (2008, 2011a).

## 3. METHODS AND RESULTS

### 3.1. CO Spectra

The $\upsilon$ = (1–0) and $\upsilon$ = (2–0) rovibrational bands are shown for all targets in Figures 1 through 6 in ascending order of $^{12}C^{16}O$ ice optical depths at ∼4.675 $\mu$m, with the main portions of the spectra used in the analysis presented. A forest of narrow CO rovibrational absorption lines is seen to varying degrees in all spectra. A magnified spectral region of HL Tau is shown as a representative example of individual line profiles (Figure 7). Broad, complex $\upsilon$ = (1–0) CO emission is often seen in the spectra and likely originates in the innermost ($R < 1$ AU) regions of the disks (Herczeg et al. 2011). However, the emission does not interfere with the analysis, as it is much broader than the absorption, and is generally weak or absent in the rare isotopologue transitions. The potentially affected $\upsilon$ = (1–0) $^{12}C^{16}O$ lines are not used for column density measurements. Broad absorption observed toward several objects at $\upsilon$ = (2–0) (Figures 5 and 6) likely originates in the stellar photosphere and is clearly separated from the narrow interstellar CO lines.

Temporal variation in $[^{12}C^{16}O]/[^{13}C^{16}O]$ was found toward VV CrA S, with a $[^{12}C^{16}O]/[^{13}C^{16}O]$ abundance ratio of 136 ± 1.3 when using a $\upsilon$ = (1–0) observation four months prior to the $\upsilon$ = (2–0), as compared to 127 ± 1 when coeval observations were used (errors are statistical 1$\sigma$ values). The

[6] http://www.atm.ox.ac.uk/RFM

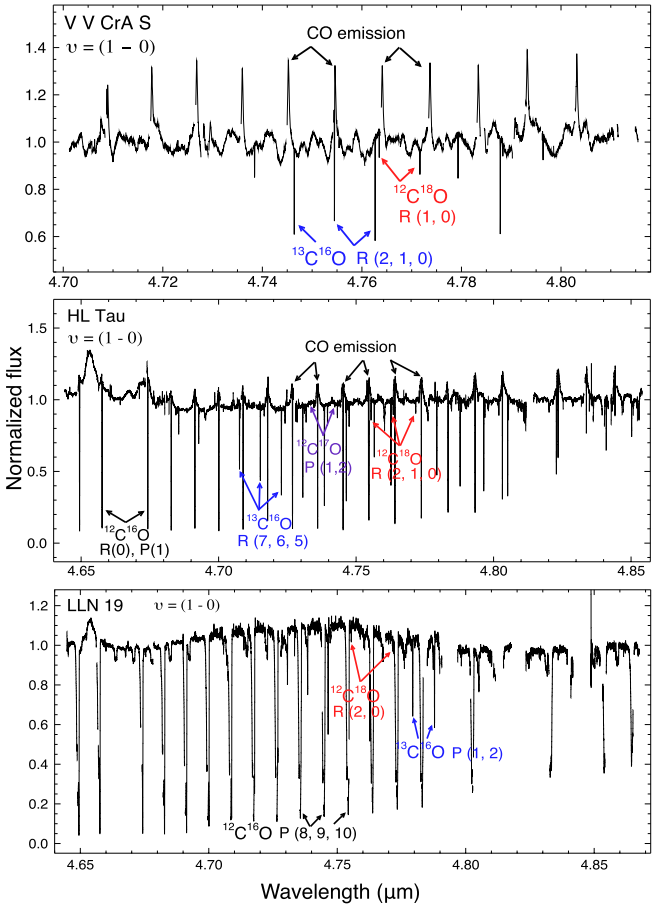


**Figure 2.** Infrared absorption spectra of the CO fundamental rovibrational band toward VV CrA S, HL Tau, and LLN 19, characterized by weak lower-limits (VV CrA S and HL Tau), or shallow (LLN 19) $^{12}C^{16}O$ ice optical depths (Table 7). HL Tau and LLN 19 have a rich CO forest of narrow rovibrational absorption lines due to the various CO isotopologues present. Sample lines are marked. Few lines of the rarer isotopologues ($^{12}C^{18}O$ and $^{12}C^{17}O$) are seen toward the more deeply embedded object, LLN 19. Low-level emission toward VV CrA S and HL Tau are possibly representative of hot CO gas of the inner disk. The weak emission line at ~4.65 $\mu$m for HL Tau and LLN 19 is HI Pfund $\beta$.

possibility of temporal spectral variability should therefore be considered for DoAr24E and IRS 63, targets for which only non-coeval observations are available.

### 3.2. Derivation of Column Densities and Isotopologue Ratios

Total abundances for each isotopologue were derived by measuring the column density of CO in each observed rovibrational level of the ground vibrational state which, in turn, was obtained from the intrinsic optical depths at line center ($\tau_o$), derived from a best-fit absorption line profile to each rovibrational transition. Individual column densities were used to make a best fit to a Boltzmann population, then summed over all levels. This method is described in detail in Smith et al. (2009).

The technique of using the line profiles to directly determine column densities takes advantage of the high spectral resolution of CRIRES to spectrally resolve the velocity dispersion of the individual CO lines. This in turn leads to greater precision than using unresolved lines, which require a curve-of-growth analysis to derive intrinsic line widths (Mitchell et al. 1989, 1990, 1991; Sheffer et al. 1992; Mitchell & Maillard 1993; Lambert et al. 1994; Sheffer et al. 2002; Federman et al. 2003; Goto et al. 2003; Brittain et al. 2005). With CRIRES, the resolving power is sufficiently high to partially resolve the intrinsic line profiles ($FWHM_{Intrinsic} \sim FWHM_{Instrumental}$), albeit marginally in some cases: VV CrA S, RNO 91, and IRS 43. Therefore, it is possible that the derived column densities toward these targets may be more uncertain.

The measured instrumental broadening, intrinsic velocity dispersions, and optical depth ranges for each observed isotopologue are shown in Table 3. Line-by-line optical depths and Doppler shifts for observed targets are available in the online version of this paper, with a sample partial line list shown in Table 4. Instrumental broadening values were modeled individually for each spectrum in its entirety, following the method in Seifahrt et al. (2010) for using an atmospheric model for telluric spectra. The RFM code was used to derive a detailed fit to the individual telluric standard star spectra, with consideration of meteorological conditions at the time of observation. The atmospheric molecular parameters were taken from the HITRAN 2008 database (Rothman et al. 2009). There are small relative differences in resolving power between the standard stars and science targets due to differences in seeing or adaptive optics (AO) correction, but these differences were accurately measured and corrected for by minimizing the continuum residuals after telluric division.

Optimized intrinsic velocity dispersions were derived from the weighted mean of dispersions measured in individual $^{12}C^{18}O$ lines, assuming that both the intrinsic and instrumental profiles are well-approximated by Gaussian profiles. The $^{12}C^{18}O$ lines were used because this rare isotopologue is always optically thin and therefore is not subjected to saturation line broadening, which may affect the more common $^{13}C^{16}O$ isotopologue. Optical depths of the optically thin $^{12}C^{16}O$ $\upsilon = (2\text{–}0)$ lines were similarly computed using the derived intrinsic broadening from the $\upsilon = (1\text{–}0)$ $^{12}C^{18}O$ lines. It can be noted that even when the resolving power of the two spectral bands differed for a single target, we obtained good fits to lines in both bands under the reasonable assumption that the intrinsic profile width is independent of transition and isotopologue. Further, it is reasonable to use the same velocity dispersion parameter for a target with a two-temperature distribution of the data, since thermal contributions are very small contributors to the total intrinsic dispersion (0.077 and 0.242 km s$^{-1}$ for $^{12}C^{16}O$ at 20 and 200 K, respectively).

The rotational analyses for all targets are shown in Figures 8 and 9. Sub-level column densities, $N_J/(2J+1)$, derived from the fits to the absorption lines, are plotted against the energy, $E/k$, of the rotational transition state, $J$. For targets where cold gas dominates, a single-temperature model is sufficient to fit the data, while targets with absorption that includes higher-$J$ transitions are best fit with a two-temperature model, representing cold and warm environments along the line of sight. The two-temperature model further allows for different excitation temperatures for each isotopologue along a given line of sight. Derived isotopologue temperatures from the fits are shown in Table 5. High temperatures (~80–250 K) are roughly consistent with those of the inner parts of typical YSO envelopes, while low temperatures (~5–30 K) may trace outer envelopes or molecular cloud material in front of the YSOs. For lines of sight with no warm component, it is likely that the gas is from a foreground cloud not related to the YSO itself (DoAr24E N and S, VV CrA S, and IRS 51).

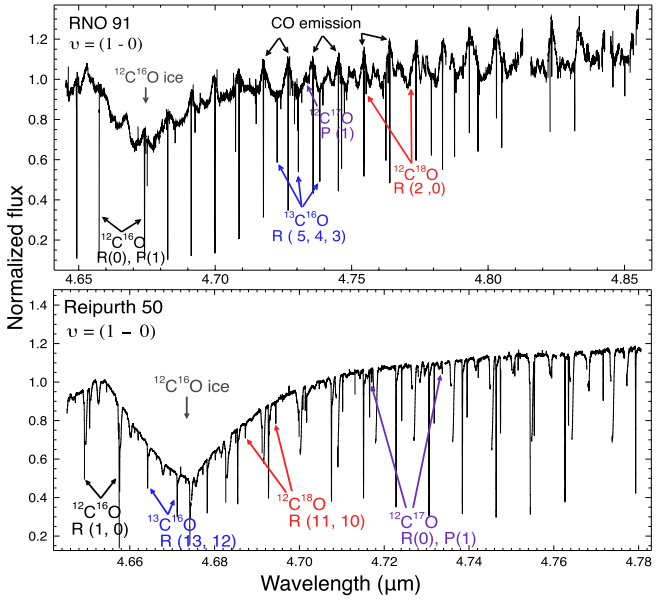


**Figure 3.** Infrared absorption spectra of the CO fundamental rovibrational band toward RNO 91 and Reipurth 50, with moderate optical depths of $^{12}C^{16}O$ ice ($\tau < 1$). The rich CO forest of narrow rovibrational absorption lines is due to the various CO isotopologues present. Sample lines are marked. RNO 91 shows low-level emission that is possibly representative of the inner disk.

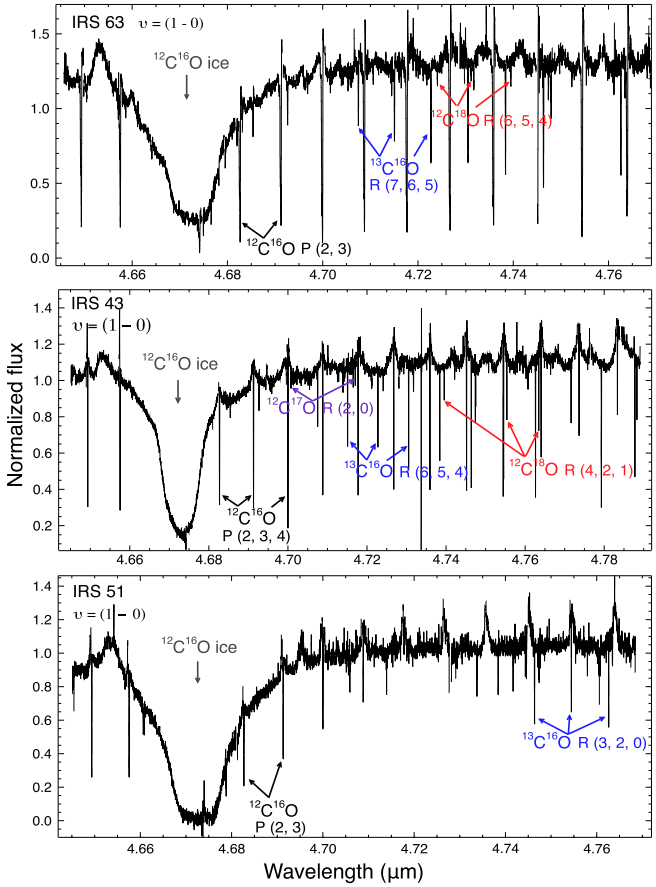


**Figure 4.** Infrared absorption spectra of the CO fundamental rovibrational band toward IRS 63, IRS 43, and IRS 51, embedded YSOs with deep $^{12}C^{16}O$ ice features. The CO absorption toward IRS 51 is particularly cold, leading to the detection of only low-$J$ transitions. Sample lines are marked. The weak emission line at ~4.65 $\mu$m is HI Pfund $\beta$.

Total column densities and isotopologue ratios are shown in Table 6. Due to the dominance of higher-$J$ lines in targets with both low- and high-temperature lines, the higher-temperature ratios are generally better constrained within two-temperature environments (Smith et al. 2009).

Our statistical errors on the column densities are generally small, reflecting the very high signal-to-noise ratio of the data. For example, the average signal-to-noise per pixel in the fundamental bands is ~250. With an average CRIRES FWHM of 2.0 pixels, we retrieve average line errors of ~0.3% ($1/(250 \times \sqrt{2.0})$). First-overtone bands average ~1%. We therefore expect to know the column densities to a fraction of a percent, which is represented in our results. These errors do not take into account any potential systematic errors in extracting the line strengths and profiles due to inherent non-Gaussianity of the line-fitting procedure, which we cannot quantify with certainty. However, to roughly estimate the magnitude of systematic retrieval errors, we carried out a small number of forward models with two-dimensional radiative transfer models (RADLite, Pontoppidan et al. 2009) simulating synthetic CO isotopologue absorption spectra using a basic one-dimensional infalling envelope from Shu (1977). The synthetic spectra were convolved with the appropriate instrumental resolution, and isotopologue ratios were then retrieved from these synthetic spectra with the same methods used for the observed data. In each case, we were able to reproduce the input ratios to better than 10%. We therefore estimate that model-dependent systematics add at most a 10% error to the retrieved isotopologue ratios, in addition to the statistical error.

### 3.3. Notes on Individual Sources

The DoAr24E system is a hierarchical multiple for which we have spectra of two components, with the rotational analyses nearly identical for both components. This lack of significant spatial variability strongly suggests that we are tracing spatially extensive and homogenous foreground material, that in turn is the dominant contributor smoothly distributed on scales of at least a few 100 AU. The lack of isotopic variability between the DoAr24E components gives us further confidence on our retrieval method for deriving precise isotope ratios.

Due to high extinction leading to a faint $\upsilon = (2–0)$ band continuum for the embedded YSO, IRS 43, we detect only low-$J$ lines for $^{12}C^{16}O$, while we find high- and low-$J$ lines for all CO isotopologues in $\upsilon = (1–0)$. Given this disparate set of temperature ranges, our data for IRS 43 are therefore not useful for measuring CO isotopologue abundance ratios relative to $^{12}C^{16}O$.

Toward VV CrA S, we derive a $^{12}C^{16}O$ column density of $1.178 \pm 0.004 \times 10^{18}\,cm^{-2}$. This is nearly three orders of magnitude higher than the value $2.6 \pm 0.4 \times 10^{15}\,cm^{-2}$ derived in Kruger et al. (2011). Our rotational temperature ($14 \pm 1$ K) is also significantly lower than their value ($29 \pm 4$ K). Since Kruger et al. (2011) used the $\upsilon = (1–0)$ spectra from the archive, these differences could be explained by strong saturation effects resulting from their use of the highly optically thick $\upsilon = (1–0)$ $^{12}C^{16}O$ lines. This difference reinforces the necessity of using $\upsilon = (2–0)$ data for deriving precise $^{12}C^{16}O$ column densities.

Smith et al. (2009) proposed that the cold gas component observed toward VV CrA S may be interpreted as either molecular cloud material in front of the VV CrA binary system, or disk gas toward the primary component as suggested by

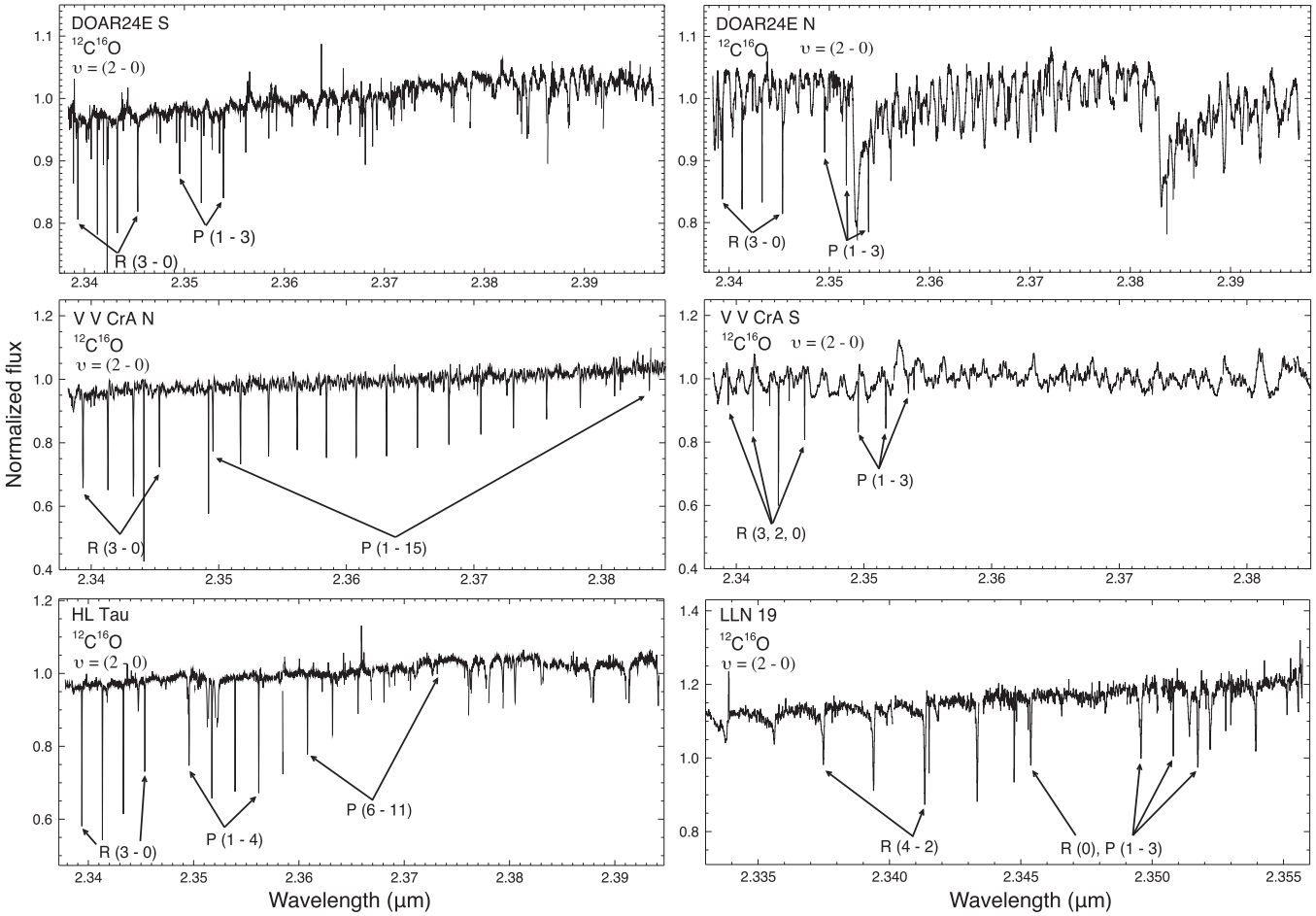


**Figure 5.** Infrared absorption spectra of the CO rovibrational first-overtone bands toward the YSOs shown in Figures 1 and 2. Several detected rovibrational $^{12}C^{16}O$ lines are marked. Broad absorption lines at ∼2.34–2.353 $\mu$m, most evident toward DoAR24E N, S, VV CrA S, and LLN 19, are due to photospheric CO.

Kruger et al. (2011). We point out that the former is more likely because the presence of both warm and cold components are expected for a disk, while a foreground cloud will typically only show a single cold component, such as that seen toward VV CrA N. Taken together, the likely geometry for the VV CrA system and the spectroscopic results render it unlikely that the VV CrA S spectra represent the outer disk. VV CrA N observations most likely represent warm and cold disk gas.

### 3.4. Carbon Isotope Ratios versus Galactocentric Radius

Derived $[^{12}C^{16}O]/[^{13}C^{16}O]$ ratios are plotted against Galactocentric radius ($R_{GC}$) in Figure 10. The solar system and local ISM values of ∼87 (Scott et al. 2006) and ∼68 (Milam et al. 2005) are plotted at 8 kpc, respectively. Derived $[^{12}C^{16}O]/[^{13}C^{16}O]$ toward our targets range from ∼85 to 165, values that are inconsistent with those toward most YSOs and molecular clouds, or those predicted from GCE (Prantzos et al. 1996) and regression models (Milam et al. 2005). The distribution of data from the literature approximates the general trend of increasing metallicity toward the Galactic center, with the corresponding increase in $^{12}C/^{13}C$ with greater $R_{GC}$.

### 3.5. Derivation of CO Ice Fractions

Previous studies have discussed the exchange between $^{12}C^{16}O$ solid- and gas-phase reservoirs in disks and envelopes (e.g., van Dishoeck et al. 1996; Boogert et al. 2000). With a range of $^{12}C^{16}O$ ice column densities centered at 4.75 $\mu$m (Figures 1 through 4), our data set provided an opportunity to investigate relationships between the gas-phase isotopologue ratios and the $^{12}C^{16}O$ ice fraction along single lines of sight. $^{12}C^{16}O$ ice column densities were calculated from optical depth analyses in Pontoppidan et al. (2003) and Thi et al. (2010).

Of the broad $^{12}C^{16}O$ ice profile, the pure, cold $^{12}C^{16}O$ component is most relevant with respect to interactions with $^{12}C^{16}O$ gas, as it is the solid state reservoir that would most likely directly exchange with the gas in cold, dense clouds. We used optical depths for this component to derive total $^{12}C^{16}O$ ice column densities for each target. From the phenomenological decomposition analysis in Pontoppidan et al. (2003), and Thi et al. (2010) for LLN 19, the pure component corresponds to the middle optical depth ($\tau_{mc}$) profile measurement. For targets with no (VV CrA, DoAr24E) or very weak (HL Tau) spectral ice features, we used upper limits from the CRIRES fundamental bands.

Total column densities of pure $^{12}C^{16}O$ in the ice phase ($N_{Pure,CDE}$) were computed using the relation from Pontoppidan et al. (2003),

$$N_{Pure,CDE} = 6.03\ cm^{-1} \times \tau_{max} \times A_{bulk}^{-1}, \quad (1)$$

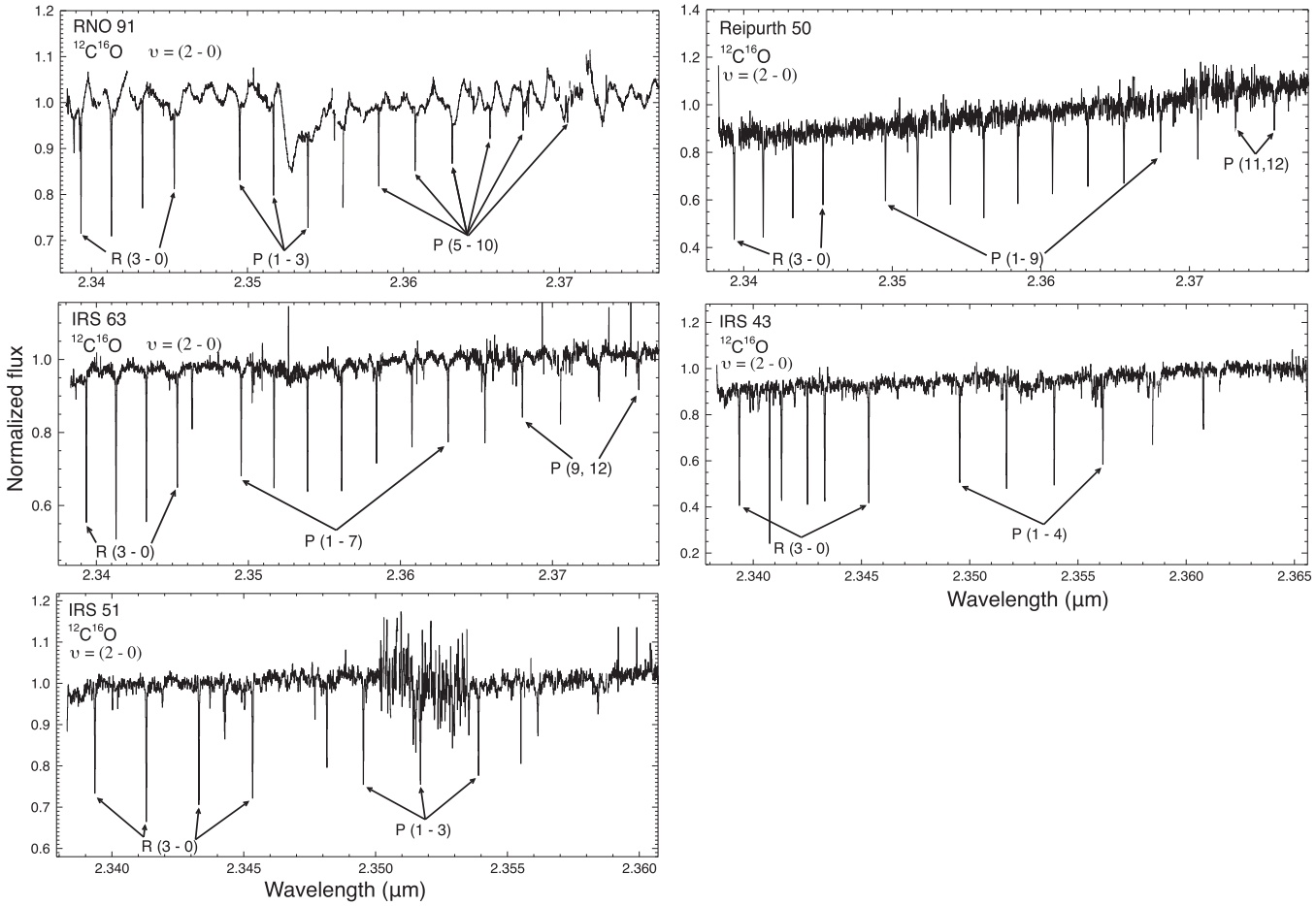


**Figure 6.** Infrared absorption spectra of the CO rovibrational first-overtone bands toward the YSOs shown in Figures 3 and 4. Several detected rovibrational $^{12}C^{16}O$ lines are marked. Broad photospheric CO lines are observed toward RNO 91 and more weakly toward IRS 63.

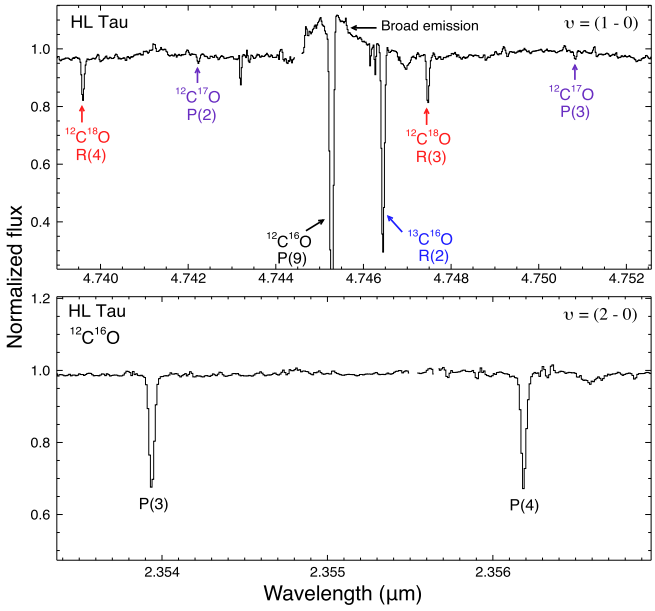


**Figure 7.** Representative magnification for fundamental (top) and first-overtone (bottom) bands, here shown for HL Tau. Isotopologue lines are marked.

where $\tau_{max}$ is the optical depth at line center of the pure $^{12}C^{16}O$ component, $A_{bulk}$ is the band strength of $^{12}C^{16}O$, and the numerical factor, 6.03 $cm^{-1}$, considers the effect of grain shape on the band strength. In this study, we used the continuous distribution of ellipsoids (CDE) model (Pontoppidan et al. 2003) for computing solid $^{12}C^{16}O$ column densities.

Optical depths, column densities, and total $^{12}C^{16}O$ ice fractions are listed in Table 7 in ascending order of $^{12}C^{16}O$ ice optical depth. Although it is assumed that cold CO gas will more likely exchange with $^{12}C^{16}O$ ice, for targets where $^{12}C^{16}O$ gas was observed in both cold and warm environments, values for $^{12}C^{16}O$ ice fractions are shown separately for each environment.

The relation between the $^{12}C^{16}O$ ice fraction and $[^{12}C^{16}O]/[^{13}C^{16}O]$ gas-phase ratios is shown in Figure 11, with $^{12}C^{16}O$ ice fractions plotted against derived $[^{12}C^{16}O]/[^{13}C^{16}O]$ for cold ($T \sim$ 5–30 K) and, where observed, warm ($T \sim$ 80–250 K) regimes. We distinguish between targets where only cold CO gas is observed, and targets where both warm and cold temperatures are found. In the latter cases, cold-gas measurements are likely more uncertain due to the contribution of the high-temperature on the low-temperature lines.

**Table 3**
Summary of Observed Line Parameters

| Target | FWHM$_{instrumental}$[a] | | FWHM$_{intrinsic}$[b] | $\tau$ ($^{12}C^{16}O$) | $\tau$ ($^{13}C^{16}O$) | $\tau$ ($^{12}C^{18}O$) | $\tau$ ($^{12}C^{17}O$) |
|---|---|---|---|---|---|---|---|
| | $M$ (km s$^{-1}$) | $K$ (km s$^{-1}$) | (km s$^{-1}$) | $v = (2-0)$ | $v = (1-0)$ | $v = (1-0)$ | $v = (1-0)$ |
| DoAr24E S | 2.79 | 3.12 | 2.33 ± 0.56 | 0.184 – 0.353 | 0.217 – 1.033 | 0.027 – 0.077 | ··· |
| DoAr24E N | 2.79 | 3.12 | 2.33 ± 0.56[c] | 0.075 – 0.330 | 0.198 – 1.014 | 0.047 – 0.068 | ··· |
| VV CrA N | 2.82 | 3.49 | 4.28 ± 0.07 | 0.064 – 0.573 | 0.568 – 1.322 | 0.095 – 0.174 | 0.020 – 0.038 |
| VV CrA S | 2.82 | 3.49 | 1.74 ± 0.12 | 0.170 – 0.614 | 0.225 – 1.377 | 0.119 – 0.228 | 0.021 – 0.034 |
| HL Tau | 3.26 | 3.43 | 2.63 ± 0.05 | 0.027 – 0.987 | 0.036 – 2.896 | 0.079 – 0.310 | 0.021 – 0.052 |
| LLN 19 | 3.22 | 4.68 | 3.52 ± 0.27 | 0.196 – 0.437 | 0.627 – 0.909 | 0.072 – 0.108 | ··· |
| RNO 91 | 3.26 | 3.72 | 1.67 ± 0.27 | 0.105 – 0.843 | 0.089 – 2.290 | 0.046 – 0.370 | 0.059 – 0.072 |
| Reipurth 50 | 3.44 | 4.54 | 3.08 ± 0.02 | 0.225 – 1.366 | 0.338 – 2.831 | 0.027 – 0.707 | 0.044 – 0.138 |
| IRS 63 | 3.57 | 3.39 | 3.83 ± 0.35 | 0.057 – 0.811 | 0.171 – 1.582 | 0.141 – 0.245 | 0.043 – 0.081 |
| IRS 43 | 3.03 | 3.45 | 1.86 ± 0.11 | 1.076 – 2.563 | 0.212 – 4.542 | 0.073 – 1.115 | 0.033 – 0.280 |
| IRS 51 | 3.03 | 3.37 | 1.88[d] | 0.504 – 0.822 | 0.739 – 1.437 | ··· | ··· |

**Notes.**
[a] The instrumental broadening is measured by fitting an atmospheric model to unresolved telluric lines. The uncertainty is $\lesssim$0.1 km s$^{-1}$. These refined measurements of instrumental broadening account for the slight variation in results for VV CrA and Reipurth 50 as compared to (Smith et al. 2009).
[b] The intrinsic velocity dispersion is the Gaussian FWHM before being convolved with the measured instrumental CRIRES broadening for the individual spectra. It is based on a weighted mean FWHM from a selection of $^{12}C^{18}O$ lines, unless otherwise noted. Uncertainties reflect the weighted means of the individual $^{12}C^{18}O$ line widths.
[c] Mean value from DoAr24E S $^{12}C^{18}O$ lines $R(2)$ and $R(1)$.
[d] This width is estimated based $^{12}C^{16}O$ and $^{13}C^{16}O$ lines, since the source has very weak $^{12}C^{18}O$ lines.

**Table 4**
Optical Depths ($\tau_o$) and Doppler Shifts for CO Isotopologue Rovibrational Lines Used in Deriving Column Densities for DoAr24E S[a,b]

| Isotopologue | Transition | $\tau_o$ | $V_{LSR}$ (km s$^{-1}$) |
|---|---|---|---|
| $^{12}C^{16}O$ | (2, 0) $R(3)$ | 0.279 ± 0.002 | 3.09 ± 0.01 |
| $^{12}C^{16}O$ | (2, 0) $R(2)$ | 0.353 ± 0.002 | 3.31 ± 0.01 |
| $^{12}C^{16}O$ | (2, 0) $R(1)$ | 0.326 ± 0.002 | 3.42 ± 0.01 |
| $^{12}C^{16}O$ | (2, 0) $R(0)$ | 0.262 ± 0.002 | 3.84 ± 0.02 |
| $^{12}C^{16}O$ | (2, 0) $P(1)$ | 0.184 ± 0.002 | 3.53 ± 0.02 |
| $^{12}C^{16}O$ | (2, 0) $P(2)$ | 0.255 ± 0.002 | 3.47 ± 0.01 |
| $^{12}C^{16}O$ | (2, 0) $P(3)$ | 0.250 ± 0.003 | 4.06 ± 0.03 |

**Notes.**
[a] Uncertainties are 1$\sigma$ derived from the line fits.
[b] This is a partial table for DoAr24E S. A complete line-by-line table for all targets observed in this study is available in machine-readable form.

(This table is available in its entirety in machine-readable form.)

### 3.6. Solid [$^{12}C^{16}O$]/[$^{13}C^{16}O$] Toward IRS 51

The optical depth for the $^{13}C^{16}O$ ice toward the foreground cloud traced by IRS 51 provides the only solid [$^{12}C^{16}O$]/[$^{13}C^{16}O$] ratio (68 ± 10; Pontoppidan et al. 2003) that can be compared to a gas-phase ratio along the same line of sight in this study. The solid-phase [$^{12}C^{16}O$]/[$^{13}C^{16}O$] ratio is significantly lower than our derived gas-phase [$^{12}C^{16}O$]/[$^{13}C^{16}O$] ratio of 165 ± 10 for IRS 51, but is roughly consistent with other published [$^{12}C^{16}O$]/[$^{13}C^{16}O$] values for ice in YSO targets; Boogert et al. (2002a) derive a [$^{12}C^{16}O$]/[$^{13}C^{16}O$] ratio of 71 ± 15 for the ice observed toward the massive YSO, NGC 7538 IRS 9, using Keck-NIRSPEC, and a ratio of 45 ± 15 was observed toward the CRBR 2422.8–3423 edge-on disk using VLT-ISAAC (Pontoppidan et al. 2005).

## 4. DISCUSSION

### 4.1. Galactic [$^{12}C^{16}O$]/[$^{13}C^{16}O$] Heterogeneity

We find significant gas-phase heterogeneity in [$^{12}C^{16}O$]/[$^{13}C^{16}O$] toward our targets (Figures 10 and 11), with most values falling above local ISM values of ∼65–69, as determined by submillimeter observations (Wilson 1999; Milam et al. 2005). The large spread in [$^{12}C^{16}O$]/[$^{13}C^{16}O$] suggests either heterogeneity in the carbon isotopic composition in our local solar neighborhood (e.g., $R_{GC} \sim 8$ kpc), and/or one or more new fractionation mechanisms for CO operating in the dense envelopes of young stars. The distribution of CO isotopologue ratios derived from our CRIRES data do not match the general Galactic trend, which suggests that the carbon reservoirs of young stellar envelopes do not necessarily isotopically represent their parent clouds, as is often assumed in GCE models (Prantzos et al. 1996).

We are not the first to observe unusual [$^{12}C^{16}O$]/[$^{13}C^{16}O$] abundance ratios in YSOs and molecular clouds (Figure 10). In ultraviolet absorption, Lambert et al. (1994) and Federman et al. (2003) found high [$^{12}C^{16}O$]/[$^{13}C^{16}O$] values toward diffuse regions in the Ophiuchus cloud, with values ranging from ∼117 to 167. These results have been attributed to selective CO photodissociation by external ultraviolet radiation (Lambert et al. 1994; Federman et al. 2003). We discuss connections with CO photodissociation in Section 4.3.

Unusually high [$^{12}C^{16}O$]/[$^{13}C^{16}O$] values were also detected in rovibrational absorption using Subaru ($\lambda/\Delta\lambda \approx$ 23,000) toward the massive young stars LkH$\alpha$101 and MonR2 IRS3, with values of ∼137 and 158, respectively (Goto et al. 2003). Goto et al. (2003) suggested that photon-trapping in the rotational lines of the most abundant isotope as a possible explanation for the apparently elevated carbon isotope ratios, although the potential effect was not quantified in their study.

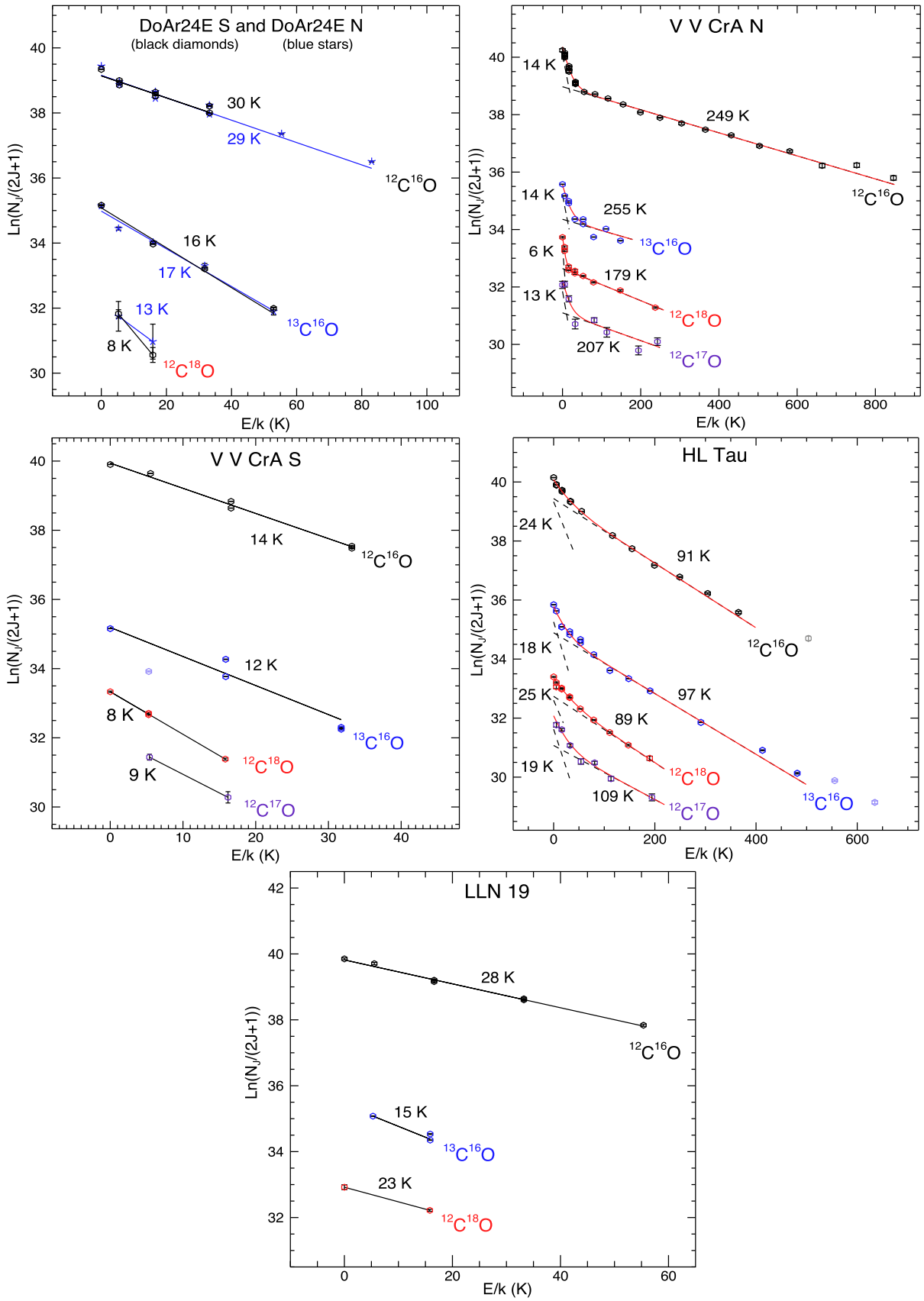


**Figure 8.** Rotational excitation diagrams for targets with little to no ice, corresponding to targets shown in Figures 1, 2, and 5). $E$ is the energy of the $J^{th}$ rotational state above the ground rotational state and $k$ is the Boltzmann constant. One- and two-temperature simultaneous fits were used as warranted by the rotational excitation structure. Derived high and low temperatures for each isotopologue are indicated on the plots. Error bars are $1\sigma$ propagated from the Gaussian fits to the line profiles. Faded symbols are outliers that have been excluded from the fits.

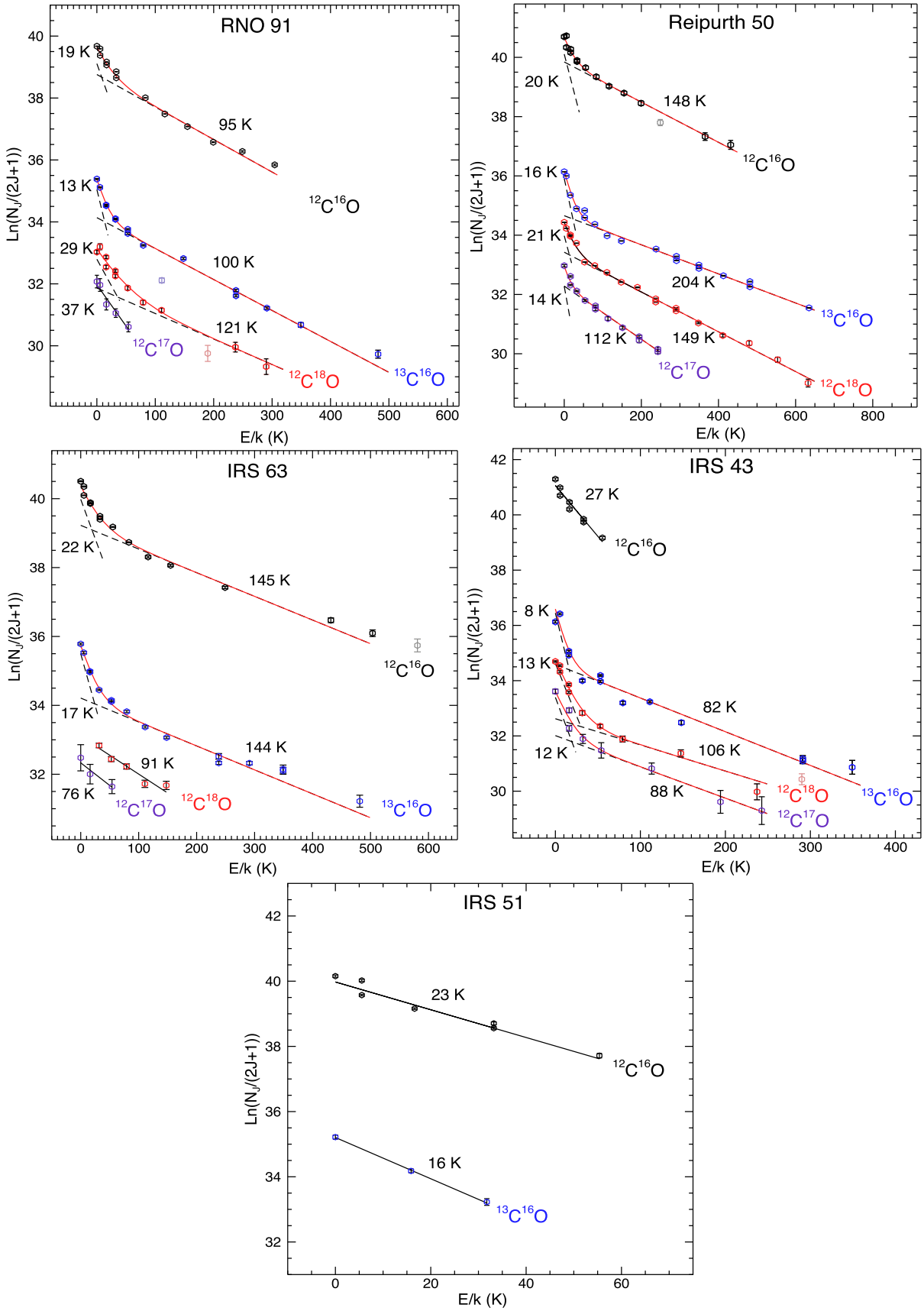


**Figure 9.** Rotational excitation diagrams for targets with moderate to deep CO ice features, corresponding to targets in Figures 3, 4, and 6. $E$ is the energy of the $J^{th}$ rotational state above the ground rotational state and $k$ is the Boltzmann constant. One- and two-temperature simultaneous fits were used as warranted by the rotational excitation structure. Derived high and low temperatures for each isotopologue are indicated on the plots. Error bars are $1\sigma$ propagated from the Gaussian fits to the line profiles. Faded symbols are outliers that have been excluded from the fits.

**Table 5**
Measured CO Isotopologue Rotational Temperatures

| Target | Component[a] | $T_{ex}(^{12}C^{16}O)$ (K) | $T_{ex}(^{13}C^{16}O)$ (K) | $T_{ex}(^{12}C^{18}O)$ (K) | $T_{ex}(^{12}C^{17}O)$ (K) |
|---|---|---|---|---|---|
| DoAr24E S | single | 30 ± 1 | 16 ± 1 | 8 ± 2 | ⋯ |
| DoAr24E N | single | 29 ± 1 | 17 ± 1 | 13 ± 12 | ⋯ |
| VV CrA N | high | 249 ± 2 | 255 ± 8 | 179 ± 5 | 207 ± 39 |
| VV CrA N | low | 14 ± 1 | 14 ± 1 | 6 ± 1 | 13 ± 3 |
| VV CrA S | single | 14 ± 1 | 12 ± 1 | 8 ± 1 | 9 ± 1 |
| HL Tau | high | 91 ± 1 | 97 ± 1 | 89 ± 6 | 109 ± 17 |
| HL Tau | low | 24 ± 1 | 18 ± 1 | 25 ± 3 | 19 ± 5 |
| LLN 19 | single | 28 ± 1 | 15 ± 1 | 23 ± 2 | ⋯ |
| RNO 91 | high | 95 ± 1 | 100 ± 1 | 121 ± 21 | ⋯ |
| RNO 91 | low | 19 ± 1 | 13 ± 1 | 29 ± 5 | 37 ± 6 |
| Reipurth 50 | high | 148 ± 8 | 204 ± 1 | 149 ± 1 | 112 ± 3 |
| Reipurth 50 | low | 20 ± 3 | 16 ± 1 | 21 ± 1 | 14 ± 1 |
| IRS 63 | high | 145 ± 3 | 144 ± 4 | 91 ± 8 | 76 ± 40 |
| IRS 63 | low | 22 ± 1 | 17 ± 1 | ⋯ | ⋯ |
| IRS 43 | high | ⋯ | 82 ± 2 | 106 ± 15 | 88 ± 21 |
| IRS 43 | low | 27 ± 1 | 8 ± 1 | 13 ± 1 | 12 ± 2 |
| IRS 51 | single | 23 ± 1 | 16 ± 1 | ⋯ | ⋯ |

**Notes.** All uncertainties are $1\sigma$ statistical errors derived from the rotational analysis.
[a] The temperature component: *single* if a single-temperature component was used; *high* and *low* for two-temperature models.

### 4.2. Ice–Gas Partitioning of $^{12}C^{16}O$ and $^{13}C^{16}O$

#### 4.2.1. Observed Relation between the Ice–Gas Fraction and the CO Isotopologue Ratios

A possible mechanism for the observed CO fractionation is mass-dependent exchange between gas and ice. Compared to single-dish, beam-averaged millimeter measurements of CO gas-phase isotopologue ratios in molecular clouds, rovibrational absorption through protostellar envelopes is likely to probe denser gas. Dense, cold gas is known to lead to efficient CO freeze-out onto dust grains (Jørgensen et al. 2004). If the adsorption/desorption rates of CO are mass-dependent, isotopologue fractionation may occur. Furthermore, if the heavier isotopologue ($^{13}C^{16}O$) is more tightly bound to the dust grains, we would expect an increased $[^{12}C^{16}O]/[^{13}C^{16}O]$ ratio in the gas, which is consistent with the detection of large columns of $^{12}C^{16}O$ ice along the observed lines of sight. Below we discuss whether ice–gas partitioning is a possible explanation for the observed high CO isotopologue ratios in the gas.

The relative fraction of CO sequestered in ice, averaged along the line of sight, is plotted against the $[^{12}C^{16}O]/[^{13}C^{16}O]$ abundance ratios in the gas (Figure 11). We might expect to find increased gas-phase $[^{12}C^{16}O]/[^{13}C^{16}O]$ ratios for lines of sight with high ice/gas fractions if $^{13}C^{16}O$ were preferentially bound in the ice mantles. Instead we see significant scatter, much larger than the individual errors on each data point, and no simple apparent relation between these quantities. A correlation is particularly absent between the cold-gas component and the CO ice fraction, although these two quantities are likely cospatial and trace the same total CO reservoir. However, the line of sight with the largest ice fraction (IRS 51) also has the high $[^{12}C^{16}O]/[^{13}C^{16}O]$ ratio in the gas. Therefore, while we cannot rule out that ice–gas partitioning could be significant in contributing to high gas-phase $[^{12}C^{16}O]/[^{13}C^{16}O]$ ratios, other factors are also likely important.

With respect to other factors affecting the gas-phase ratios, we note that high $[^{12}C^{16}O]/[^{13}C^{16}O]$ ratios are also observed in the warm gas in some lines of sight (Figure 11, red diamonds). This finding is unexpected under the assumption that ice–gas partitioning is the only fractionation mechanism, since environments warm enough to fully sublimate the CO ice should reset the gas isotopologue fraction back to the canonical value of ∼65. In order to reconcile this result with ice–gas partitioning, there must be a mechanism to effectively remove CO from the ice during the cold phase of envelope evolution. Chemical pathways removing CO from the ice include the successive hydrogenation of CO to formaldehyde ($H_2CO$) and methanol ($CH_3OH$) (Watanabe & Kouchi 2002; Hidaka et al. 2004; Cuppen et al. 2009; Fuchs et al. 2009), or reactions with OH or O to form $CO_2$ (Mennella et al. 2006; Oba et al. 2010; Ioppolo et al. 2011). Further, we would expect the column densities of ice to be comparable or larger than those of the gas in order for the ice to be a significant reservoir that could increase the gas-phase $[^{12}C^{16}O]/[^{13}C^{16}O]$. For IRS 51, the large discrepancy in $[^{12}C^{16}O]/[^{13}C^{16}O]$ between the ice (∼68) and the gas (∼165), along with a seemingly low CO ice fraction (∼0.60), suggests instead that open-system chemistry may be occurring via CO ice reactions.

While the data are inconclusive with regard to carbon isotopic fractionation between reservoirs of CO ice and gas, potential trends in cold- and warm-gas reservoirs can be further investigated with high-resolution spectroscopy for a larger sample of protostellar lines of sight. Furthermore, models considering chemical evolution in protoplanetary environments including YSOs could consider interactions between ice and gas reservoirs as a potential influence on isotope partitioning.

#### 4.2.2. Comparison to Theoretical and Experimental Studies

To estimate whether there is an expectation of ice–gas partitioning for CO, we briefly review the theoretical basis for a potential mass dependence in the ice–gas balance. Following a standard approach for ice–gas partitioning (e.g., Tielens &

**Table 6**
Derived $^{12}C^{16}O$ Isotopologue Column Densities and Isotopologue Ratios

| Target | Comp. | $N(^{12}C^{16}O)$ ($10^{18}$ cm$^{-2}$) | $[^{12}C^{16}O]/[^{13}C^{16}O]$ | $[^{12}C^{16}O]/[^{12}C^{18}O]$ | $[^{12}C^{16}O]/[^{12}C^{17}O]$ | $[^{12}C^{18}O]/[^{12}C^{17}O]$ |
|---|---|---|---|---|---|---|
| DoAr24E S | single | 1.098 ± 0.005 | 98 ± 1 | :2500 ± 560 | ··· | ··· |
| DoAr24E N | single | 1.094 ± 0.003 | 102 ± 3 | :2200 ± 1620 | ··· | ··· |
| VV CrA N | high | 7.618 ± 0.074 | 95 ± 1 | 740 ± 15 | 3085 ± 440 | 4.1 ± 0.6 |
| VV CrA N | low | 1.413 ± 0.023 | 127 ± 2 | 1750 ± 70 | 4000 ± 630 | 2.3 ± 0.4 |
| VV CrA S | single | 1.178 ± 0.004 | 127 ± 1 | :1150 ± 20 | :3850 ± 580 | 3.4 ± 0.5 |
| HL Tau | high | 4.467 ± 0.064 | 85 ± 1 | 795 ± 80 | 3500 ± 660 | 4.4 ± 0.9 |
| HL Tau | low | 1.067 ± 0.016 | 74 ± 1 | 760 ± 80 | 2670 ± 370 | 3.5 ± 0.6 |
| LLN 19 | single | 2.020 ± 0.034 | 137 ± 3 | :1150 ± 90 | ··· | ··· |
| RNO 91[a] | high | 2.364 ± 0.032 | 92 ± 2 | 740 ± 210 | 2170 ± 280 | 2.9 ± 0.9 |
| RNO 91[a] | low | 0.689 ± 0.007 | 80 ± 2 | 350 ± 40 | 630 ± 80 | 1.8 ± 0.3 |
| Reipurth 50 | high | 10.81 ± 0.766 | 124 ± 9 | 580 ± 40 | 2480 ± 200 | 4.3 ± 0.2 |
| Reipurth 50 | low | 1.976 ± 0.157 | 76 ± 6 | 420 ± 30 | 3470 ± 380 | 8.2 ± 0.6 |
| IRS 63 | high | 5.743 ± 0.151 | 145 ± 6 | 690 ± 60 | 1830 ± 510 | 2.6 ± 0.8 |
| IRS 63 | low | 1.904 ± 0.026 | 110 ± 3 | ··· | ··· | ··· |
| IRS 43[b] | high | 6.908 ± 0.158 | :210 ± 10 | :1160 ± 180 | :2600 ± 960 | 2.2 ± 0.9 |
| IRS 43[b] | low | ··· | :300 ± 10 | :1200 ± 40 | :4500 ± 580 | :3.7 ± 0.5 |
| IRS 51 | single | 2.026 ± 0.036 | 165 ± 10 | ··· | ··· | ··· |
| Local ISM[c] | ··· | ··· | 69 ± 6 | 557 ± 30 | 2005 ± 155 | 3.6 ± 0.2 |

**Notes.** All uncertainties are 1$\sigma$ statistical errors derived from the line fits. Isotope ratios that may be affected by significant systematic uncertainty are indicated with a ":".

[a] The $^{12}C^{17}O$ lines for RNO 91 were fit with a single-temperature model.

[b] Ratios relative to $^{12}C^{16}O$ are uncertain because only low-$J$ $^{12}C^{16}O$ lines are available, while the low-$J$ lines for the other isotopologues are poorly constrained.

[c] Values from Wilson (1999).

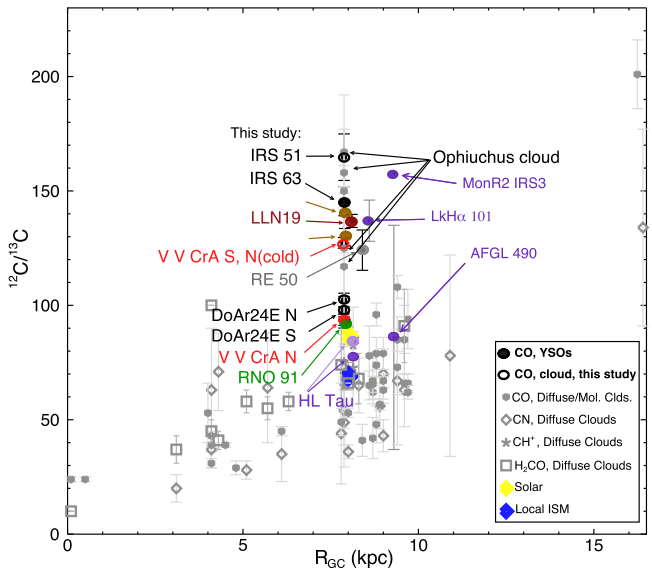


**Figure 10.** Compilation of $^{12}C/^{13}C$ ratios vs. $R_{GC}$ (kpc). Gray symbols show $^{12}C/^{13}C$ values from the literature, derived from different carbon-bearing molecules, CO, CN, $CH^+$, and $H_2CO$. Data from our study are labeled for YSO targets (filled circles) and foreground clouds (unfilled circles). Colors connect these data by molecular cloud with those in Figure 13. For targets where there is both warm and cold gas along a line of site, ratios are shown for the more robustly determined warm gas, unless otherwise noted. Local ISM (68 ± 15; Milam et al. 2005) and solar system values (86.8 ± 3.8; Scott et al. 2006) are noted. The black arrows indicate high $^{12}C/^{13}C$ in diffuse regions of Ophiuchus (Lambert et al. 1994; Federman et al. 2003). YSO data for MonR2 IRS3, LkH $\alpha$101, AFGL 490 (Goto et al. 2003), and HL Tau (lower value; Brittain et al. 2005) are marked (dark purple).

Hagen 1982), CO separations between the solid- and gas-phase reservoirs can be investigated with respect to mass-dependent kinetics and the balance between the rates of $^{12}C^{16}O$ and $^{13}C^{16}O$ gas adsorption and desorption, as given by the relation,

$$\frac{dn_{\rm ice}}{dt} = R_{\rm ads} - R_{\rm des}, \quad (2)$$

where $n_{\rm ice}$ is the number density of ice,

$$R_{\rm des} = \nu_0 \exp(-\Delta H/kT) \times n_{\rm CO,ice} \times \beta,$$

and

$$R_{\rm ads} = n_{\rm CO,gas} \times n_{\rm dust} \times \pi d^2 \times \sqrt{3kT/m_{\rm CO}} \times f$$

are the desorption and adsorption rates, respectively. The factor, $\Delta H$, is the binding energy of CO. The factor $\beta$ accounts for CO desorbing only from the top monolayer of the ice, $d$ is the grain radius, and $f$ is the sticking coefficient. The mass of CO ($m_{\rm CO}$) is an obvious mass-dependency of this relation, and $\nu_0$ is the pre-exponential factor. The number densities of the CO gas and dust particles are given by $n_{\rm CO,gas}$ and $n_{\rm dust}$, respectively (Pontoppidan 2006). In addition to the mass itself, the binding energy and pre-exponential factors are likely both mass-dependent, although to unknown degrees.

Some experimental work exists for the mass dependence of thermal desorption of CO. In an ultra-high vacuum, temperature-programmed desorption (TPD) experiment, Acharyya et al. (2007) measured binding energies and pre-exponentials for desorption from pure $^{12}C^{16}O$ and $^{13}C^{16}O$ ices. The parameters were derived using an empirical kinetic

**Table 7**
CO Ice Profile Optical Depths, Column Densities, and Ice Fractions for the CRIRES Targets[a,b]

| Target | Component | $\tau_{mc}$ | $[^{12}C^{16}O]_{Ice}$ ($10^{18}$ cm$^{-2}$) | $[^{12}C^{16}O]_{Gas}$ ($10^{18}$ cm$^{-2}$) | CO Ice Fraction[c] |
|---|---|---|---|---|---|
| DoAr24E S[d] | single | <0.02 | <0.01 | 1.10 ± 0.005 | <0.01 |
| DoAr24E N[d] | single | <0.02 | <0.01 | 1.09 ± 0.003 | <0.01 |
| VV CrA N[d] | low | <0.05 | <0.03 | 1.41 ± 0.02 | <0.02 |
| VV CrA N[d] | high | <0.05 | <0.03 | 7.62 ± 0.07 | <0.004 |
| VV CrA S[d] | single | <0.05 | <0.03 | 1.18 ± 0.004 | <0.03 |
| HL Tau[d] | low | <0.08 | <0.05 | 1.07 ± 0.02 | <0.05 |
| HL Tau[d] | high | <0.08 | <0.05 | 4.47 ± 0.06 | <0.01 |
| LLN 19[e] | single | 0.03 ± 0.002 | 0.02 ± 0.001 | 2.02 ± 0.03 | 0.01 ± 0.001 |
| RNO 91 | low | 0.25 ± 0.01 | 0.17 ± 0.004 | 0.69 ± 0.07 | 0.19 ± 0.005 |
| RNO 91 | high | 0.25 ± 0.01 | 0.17 ± 0.004 | 2.36 ± 0.03 | 0.07 ± 0.002 |
| Reipurth 50 | low | 0.51 ± 0.003 | 0.34 ± 0.002 | 1.98 ± 0.16 | 0.15 ± 0.01 |
| Reipurth 50 | high | 0.51 ± 0.003 | 0.34 ± 0.002 | 10.8 ± 0.77 | 0.03 ± 0.002 |
| IRS 63 | low | 1.69 ± 0.01 | 1.12 ± 0.01 | 1.90 ± 0.03 | 0.37 ± 0.004 |
| IRS 63 | high | 1.69 ± 0.01 | 1.12 ± 0.01 | 5.74 ± 0.15 | 0.16 ± 0.004 |
| IRS 51 | single | 4.54 ± 0.05 | 3.01 ± 0.03 | 2.03 ± 0.04 | 0.60 ± 0.01 |

**Notes.**
[a] Optical depths for all targets excepting LLN 19 are derived from the middle component as determined by the phenomenological decompositions in Pontoppidan et al. (2003).
[b] Uncertainties are $1\sigma$.
[c] $[^{12}C^{16}O]_{Ice}/([^{12}C^{16}O]_{Ice} + [^{12}C^{16}O]_{Gas}$.
[d] Upper limits on the CO ice column from spectra in this paper.
[e] Optical depth is from the middle component values from the phenomenological decompositions in Thi et al. (2010).

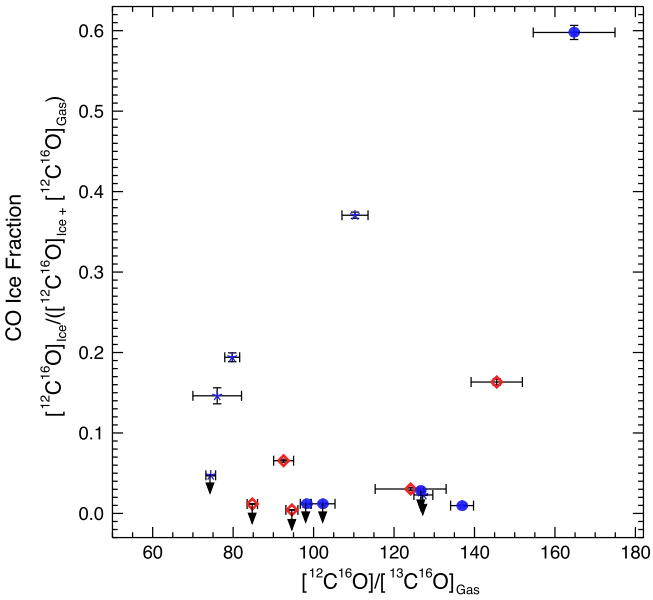


**Figure 11.** Comparison of the total $^{12}C^{16}O$ ice fraction with the $[^{12}C^{16}O]/[^{13}C^{16}O]$ gas-phase ratios for targets observed in this study. For targets where both warm and cold gas was observed, CO ice fractions are plotted with red diamonds when warm gas was used in computing the fraction, and blue stars when cold gas was used. For targets where only cold gas was observed, CO ice fractions are shown with overplotted blue ovals. Errors are $1\sigma$ propagated from errors in ice and gas optical depths measurements. $3\sigma$ upper limits (down-facing arrows) are shown for DoAr24E N, S, VV CrA N, S, and HL Tau.

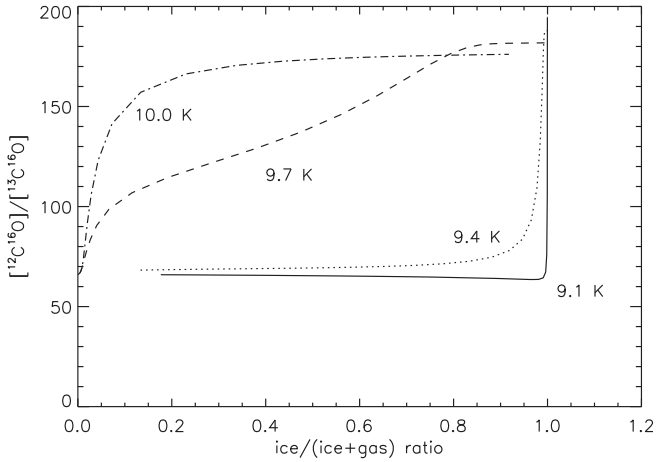


**Figure 12.** Gas-phase $[^{12}C^{16}O]/[^{13}C^{16}O]$ ratio predicted by the simple model described by Equation (2), assuming a difference in binding energy of 10 K between the two isotopologues, as allowed by the experimental uncertainty, and a pre-exponential that scales with $m_{CO}^{-1/2}$. The model is a snapshot at $5 \times 10^5$ years and the individual curves are created by varying the gas density from $10^3$ to $10^6$ cm$^{-3}$ and the temperature from 9.1 to 10.0 K, as indicated.

model. However, no difference between the $^{12}C^{16}O$ and $^{13}C^{16}O$ binding energies could be measured within the experimental uncertainties: 858 ± 15 K and 854 ± 10 K for $^{12}C^{16}O$ and $^{13}C^{16}O$, respectively.

To estimate the degree of ice–gas fractionation allowed by the boundaries imposed by the experimental evidence, we solved for the ice abundance in Equation (2), assuming a 10 K difference in binding energy between the two CO isotopologues and a pre-exponential that scales as $m_{CO}^{-1/2}$ (Hasegawa et al. 1992). In Figure 12 it is seen that, under these assumptions, the $[^{12}C^{16}O]/[^{13}C^{16}O]$ gas ratio may reach values as high as 170, but only for a narrow range of temperatures close to those of CO desorption (above which no ice exists). Essentially, a dust temperature exists at which $^{13}C^{16}O$ can efficiently remain bound to the dust surface, while $^{12}C^{16}O$ cannot. Nearly all of this effect is due to the assumed difference of only 10 K in the binding energies. Compared to what is

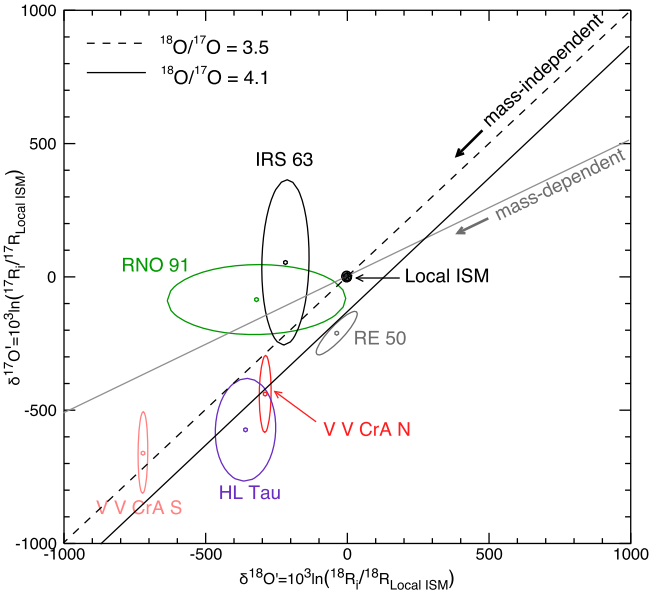


**Figure 13.** Comparison of oxygen isotope ratios between the interstellar medium and CO surrounding the targets in our study where three oxygen isotopes were observed. Oxygen isotope ratios are plotted in linearized delta notation, such that the $[^{16}O]/[^{17}O]$ and $[^{16}O]/[^{18}O]$ from local ISM values are shown in per mil using the linearized form of the delta notation. Here, $\delta^{18}O' = 10^3\ln(^{18}R_i/^{18}R_{\rm Local\ ISM})$ and $^{18}R_i = [^{12}C^{18}O]/[^{12}C^{16}O]$. Ratios for the YSOs are derived from the best-constrained (high- or single-$T$) values from the rotational analyses (Table 6). The solid and dashed lines show mass-independent fractionation (slope $\sim$ 1) lines with different assumptions for the $^{18}O/^{17}O$ ratio, as indicated. The mass-dependent line (slope $\sim$ 1/2) is also shown for comparison. Ellipses represent 65% confidence limits (standard deviation) derived from 1$\sigma$ errors from the $\tau_o$ for each line. Targets are colored according to their parent cloud (see also Figure 10).

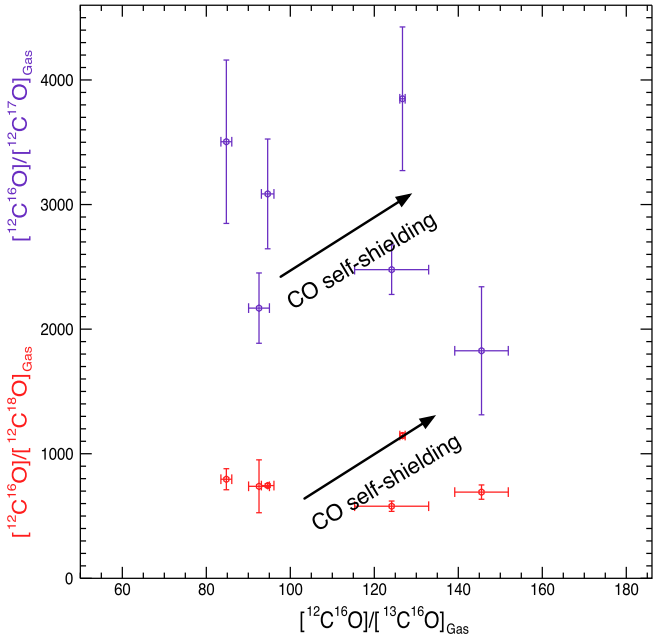


**Figure 14.** Carbon isotope ratios against oxygen isotopic abundances in targets where all isotopologues of CO were observed. The $[^{12}C^{16}O]/[^{12}C^{17}O]$ ratio is shown in purple and $[^{12}C^{16}O]/[^{12}C^{18}O]$ is shown in red. The derived $[^{16}O]/[^{17}O]$ changes by nearly a factor of two relative to $[^{12}C^{16}O]/[^{13}C^{16}O]$, while the $[^{16}O]/[^{18}O]$ varies by roughly 1.5 times with $[^{12}C^{16}O]/[^{13}C^{16}O]$. The arrows indicate the relative trends we would expect if isotopologue-specific photodissociation by CO self-shielding were the predominant process affecting the oxygen and carbon isotope ratios.

currently available, significantly more precise laboratory measurements of mass-dependent binding energies would be needed to rule out binding-energy differences as a significant cause of ice–gas fractionation. While such temperature-dependent fractionation may be consistent with the observed spread in isotopologue ratios, it remains unclear to which degree the physical conditions of real molecular clouds and envelopes must be fine-tuned to lead to significant ice–gas fractionation.

More realistic modeling of ice–gas fractionation of CO is potentially complicated by several factors. For example, investigations of the effects of CO entrapment in the ice on the desorption and adsorption (both potential mass-dependent processes) in astrophysical environments have shown that the diffusion of CO into the porous $H_2O$ ice leads to competing CO entrapment and diffusion effects on the desorption of CO, the degree to which depends on the ice temperature (Collings et al. 2003). Furthermore, a recent study has shown that three-phase modeling of $H_2O$:$CO_2$ ice desorption depends on the ice thickness and mixing ratios, which may have significant effects on ice desorption (Fayolle et al. 2011).

### 4.3. Oxygen Isotopologues and CO Self-shielding

Isotope-selective photodissociation of CO due to self-shielding refers to the differential shielding of CO isotopologues from photodissociation by far-ultraviolet (FUV) radiation in proportion to their column densities. With regard to oxygen isotopes, this leads to spatial regions characterized by more rapid destruction of $^{12}C^{17}O$ and $^{12}C^{18}O$ compared to the much more abundant $^{12}C^{16}O$ molecule. Oxygen liberated during this process is thought to eventually end up in $H_2O$, providing an explanation for the overabundance of $H_2^{18}O$ and $H_2^{17}O$ relative to $H_2^{16}O$ in the early solar system. Isotope-selective photodissociation of CO due to self-shielding has been shown to be a relevant process in the ISM (van Dishoeck & Black 1988; Visser et al. 2009).

The solar system oxygen isotope anomaly is characterized by the mass-independent correlation between $[^{16}O]/[^{18}O]$ and $[^{16}O]/[^{17}O]$ found in meteoritic materials as compared to the mass-dependent distribution known in terrestrial rocks. Mass independence refers to relative differences in $[^{16}O]/[^{18}O]$ and $[^{16}O]/[^{17}O]$ among primitive rocky objects that are nearly identical, suggesting changes in $[^{16}O]$ relative to both $[^{17}O]$ and $[^{18}O]$, rather than the expected mass-dependent trend in which relative changes in $[^{16}O]/[^{17}O]$ are about half those in $[^{16}O]/[^{18}O]$ on a log scale. The solar system oxygen anomaly has defied conclusive explanation since its discovery (Clayton et al. 1973) and has been investigated observationally by Brittain et al. (2005) and Smith et al. (2009), the latter study finding mass-independent signatures in oxygen isotopes observed in CO toward the VV CrA N disk, consistent with isotope-specific photodissociation by CO self-shielding.

The compiled oxygen data for this study, which also include refined analyses of VV CrA N and Reipurth 50 from Smith et al. (2009), are shown in Table 6 and Figure 13. The mass-dependent lines in Figure 13 are derived by estimating the oxygen isotope ratios for the ISM as a function of distance from the Galactic center. These values can be estimated from the 4 and 8 kpc values (Wilson 1999), such that for $[^{16}O]/[^{18}O]$:

$$\left[^{16}O\right]/\left[^{18}O\right]_{R_{GC}} = (57.5 \pm 10)\ R_{GC} + 97, \qquad (3)$$

where the $1\sigma$ uncertainty in the slope reflects the uncertainty in the standard errors reported in Table 4 of Wilson (1999). For $[^{16}O]/[^{17}O]$, Equation (3) is combined with values for $[^{18}O]/[^{17}O]$ in the ISM, which vary from 3.5 (Wilson 1999) to 4.1 (Wouterloot et al. 2008) (Figure 13).

We find a mass-independent signature in the oxygen isotopes relative to solar system abundances, consistent with CO self-shielding, toward the HL Tau disk, and the same mass-independent signature is retrieved in the refined results for VV CrA N (as compared to Smith et al. 2009). These findings lend further support for models considering CO self-shielding on disk surfaces (Lyons & Young 2005; Young et al. 2008). It is particularly interesting to note that the recent suggestions of planet formation in the HL Tau disk based on new ALMA imaging (Tamayo et al. 2015) would imply that CO self-shielding may be a process that occurs and/or persists later in the evolution of YSOs than previously thought.

We would not expect UV photolysis to be a significant process in the foreground cloud traced by VV CrA S or in the relatively embedded objects, RNO 91, Reipurth 50, and IRS 63. Nevertheless, due to the errors in the rare isotopologue, $^{12}C^{17}O$, a mass-dependent effect cannot be distinguished from mass-independence in oxygen fractionation for RNO 91 and IRS 63. Additional high-quality CO data for YSOs would help in evaluating mass-independence in oxygen for objects in various stages of evolution.

With regard to the rare CO isotopologues, with the exception of low-temperature gas in Reipurth 50, the $[^{12}C^{18}O]/[^{12}C^{17}O]$ ratios are within $1\sigma$–$2\sigma$ of molecular cloud radio measurements for the local ISM, further strengthening the claim that the solar system is anomalous in $^{18}O/^{17}O$ with respect to the local solar neighborhood (Young et al. 2011). This consistency in our data is observational support for $^{12}C^{18}O$ and $^{12}C^{17}O$ being similarly affected in young stellar environments.

#### 4.3.1. Evaluation of CO Self-shielding on Carbon Isotope Ratios

While critical evaluation of mass-independence requires three isotopes, we qualitatively considered if isotope-selective photodissociation by CO self-shielding could be affecting the derived $[^{12}C^{16}O]/[^{13}C^{16}O]$ toward our targets by comparing the oxygen and carbon isotope ratios where this was possible: VV CrA N, VV CrA S, HL Tau, RNO 91, Reipurth 50, and IRS 63. These are plotted in Figure 14, with the qualitative relative trend for CO self-shielding overplotted on the data. The derived $[^{12}C^{16}O]/[^{12}C^{17}O]$ changes by nearly a factor of two relative to $[^{12}C^{16}O]/[^{13}C^{16}O]$, while the $[^{12}C^{16}O]/[^{12}C^{18}O]$ varies by roughly 1.5 times with $[^{12}C^{16}O]/[^{13}C^{16}O]$. If CO self-shielding were the dominant mechanism, we would expect at least positive, direct changes in the carbon with the oxygen isotopes along an integrated line of sight, as well as similar variability in $[^{12}C^{18}O]$ and $[^{12}C^{17}O]$ compared with $[^{12}C^{16}O]/[^{13}C^{16}O]$ due to their similar rates of photodissociation (e.g., van Dishoeck & Black 1988; Visser et al. 2009). Therefore, while we cannot be certain that photodissociation of CO has no affect on the $[^{12}C^{16}O]/[^{13}C^{16}O]$, we cannot claim that it is a dominant process affecting this carbon reservoir.

Models for low-mass YSOs predict that $[^{12}C^{16}O]/[^{13}C^{16}O]$ should not increase significantly due to photodissociation (e.g., Visser et al. 2009; Woods & Willacy 2009). Atomic carbon liberated by CO photodissociation is photoionized largely to $C^+$, and $C^+$ reacts rapidly to exchange carbon with CO by the reaction $^{13}C^+ + {}^{12}CO \rightleftarrows {}^{12}C^+ + {}^{13}CO + 35$ K (Langer et al. 1984; van Dishoeck & Black 1988; Warin et al. 1996), driving $^{13}C$ back into CO and diminishing the signature of selective photodissociation. However, very high $[^{12}C^{16}O]/[^{13}C^{16}O]$ ratios derived for diffuse clouds have been attributed to CO self-shielding. Values of ~117, 125 (Federman et al. 2003), and 164 (Lambert et al. 1994) have been observed toward diffuse Ophiuchus clouds that are thought to be subjected to high-UV fields; here, CO photodissociation is thought to dominate over the carbon exchange reaction that would otherwise erase a photochemical signature.

While the upper range in $[^{12}C^{16}O]/[^{13}C^{16}O]$ in our sample is consistent with the Ophiuchus data (Figure 10), we do not find the expected mass-independent signatures in oxygen isotopes consistent with CO self-shielding. Furthermore, compared to diffuse clouds, we would not expect the molecular gas deep inside embedded YSO envelopes to be subjected to such high-UV fields given their relatively high values of visual extinction ($A_v \sim 10$; e.g., Vuong et al. 2003).

## 5. CONCLUSIONS

Heterogeneous $[^{12}C^{16}O]/[^{13}C^{16}O]$ gas-phase abundance ratios, with several unusually high values, have been found using infrared absorption spectroscopy at very high spectral resolution toward a sample of YSOs in nearby star-forming clouds. A possible partial explanation for this trend may be CO isotopologue partitioning between the ice and gas reservoirs. The degree of partitioning and the preservation of the relation in warm regions where the CO ice has sublimated would require the action of a process that can remove CO from the ice phase without returning it to the gas. Additional high-quality data could help substantiate these findings.

Signatures consistent with isotopologue-selective photodissociation by CO self-shielding were observed in the oxygen isotopes toward the disks, HL Tau and VV CrA. However, our results do not support CO self-shielding as a dominant mechanism for explaining the trends in gas-phase $[^{12}C^{16}O]/[^{13}C^{16}O]$ heterogeneity.

We conclude that chemical evolution models for young stellar environments should consider interactions between CO ice and gas reservoirs as potential fractionation mechanisms affecting the carbon isotope budget and influencing carbon isotopic heterogeneity in the gas. Interactions between these reservoirs could also contribute to isotopic heterogeneity between solar-type YSOs and their parent clouds. Finally, isotopologue-selective photodissociation by CO self-shielding should be considered an important mechanism affecting the oxygen isotopes in protoplanetary disks, potentially persisting during the later stages of planet formation.

This research was supported in part by a grant from the NASA Origins Program (E.D.Y., M.R.M., R.L.S.). This work is based on observations collected at the European Southern Observatory Very Large Telescope under program ID 179.C-0151. Support from the STScI Directors Discretionary Fund is gratefully acknowledged.

## REFERENCES

Acharyya, K., Fuchs, G. W., Fraser, H. J., van Dishoeck, E. F., & Linnartz, H. 2007, A&A, 466, 1005
Bally, J., & Langer, W. D. 1982, ApJ, 255, 143
Boogert, A. C. A., Blake, G. A., & Tielens, A. G. G. M. 2002a, ApJ, 577, 271

Boogert, A. C. A., Ehrenfreund, P., Gerakines, P. A., et al. 2000, A&A, 353, 349
Boogert, A. C. A., Hogerheijde, M. R., & Blake, G. A. 2002b, ApJ, 568, 761
Brittain, S. D., Rettig, T. W., Simon, T., & Kulesa, C. 2005, ApJ, 626, 283
Casassus, S., Stahl, O., & Wilson, T. L. 2005, A&A, 441, 181
Clayton, D. D., & Nittler, L. R. 2004, ARA&A, 42, 39
Clayton, R. N., Grossman, L., & Mayeda, T. K. 1973, Sci, 182, 458
Collings, M. P., Dever, J. W., Fraser, H. J., McCoustra, M. R. S., & Williams, D. A. 2003, ApJ, 583, 1058
Coplen, T. B., Böhlke, J. K., De Bièvre, P., et al. 2002, PApCh, 74, 1987
Cuppen, H. M., van Dishoeck, E. F., Herbst, E., & Tielens, A. G. G. M. 2009, A&A, 508, 275
Dickman, R. L. 1978, ApJS, 37, 407
Fayolle, E. C., Öberg, K. I., Cuppen, H. M., Visser, R., & Linnartz, H. 2011, A&A, 529, A74
Federman, S. R., Lambert, D. L., Sheffer, Y., et al. 2003, ApJ, 591, 986
Fuchs, G. W., Cuppen, H. M., Ioppolo, S., et al. 2009, A&A, 505, 629
Goto, M., Usuda, T., Takato, N., et al. 2003, ApJ, 598, 1038
Hasegawa, T. I., Herbst, E., & Leung, C. M. 1992, ApJS, 82, 167
Herczeg, G. J., Brown, J. M., van Dishoeck, E. F., & Pontoppidan, K. M. 2011, A&A, 533, A112
Hidaka, H., Watanabe, N., Shiraki, T., Nagaoka, A., & Kouchi, A. 2004, ApJ, 614, 1124
Ioppolo, S., van Boheemen, Y., Cuppen, H. M., van Dishoeck, E. F., & Linnartz, H. 2011, MNRAS, 413, 2281
Jørgensen, J. K., Schöier, F. L., & van Dishoeck, E. F. 2004, A&A, 416, 603
Koresko, C. D., Herbst, T. M., & Leinert, C. 1997, ApJ, 480, 741
Kruger, A. J., Richter, M. J., Carr, J. S., et al. 2011, ApJ, 729, 145
Lambert, D. L., Sheffer, Y., Gilliland, R. L., & Federman, S. R. 1994, ApJ, 420, 756
Langer, W. D., Graedel, T. E., Frerking, M. A., & Armentrout, P. B. 1984, ApJ, 277, 581
Langer, W. D., & Penzias, A. A. 1993, ApJ, 408, 539
Lyons, J. R., & Young, E. D. 2005, Natur, 435, 317
Mennella, V., Baratta, G. A., Palumbo, M. E., & Bergin, E. A. 2006, ApJ, 643, 923
Milam, S. N., Savage, C., Brewster, M. A., Ziurys, L. M., & Wyckoff, S. 2005, ApJ, 634, 1126
Mitchell, G. F., Curry, C., Maillard, J.-P., & Allen, M. 1989, ApJ, 341, 1020
Mitchell, G. F., & Maillard, J.-P. 1993, ApJL, 404, L79
Mitchell, G. F., Maillard, J.-P., Allen, M., Beer, R., & Belcourt, K. 1990, ApJ, 363, 554
Mitchell, G. F., Maillard, J.-P., & Hasegawa, T. I. 1991, ApJ, 371, 342
Oba, Y., Watanabe, N., Kouchi, A., Hama, T., & Pirronello, V. 2010, ApJL, 712, L174
Pontoppidan, K. M. 2006, A&A, 453, L47
Pontoppidan, K. M., Blake, G. A., & Smette, A. 2011a, ApJ, 733, 84
Pontoppidan, K. M., Blake, G. A., van Dishoeck, E. F., et al. 2008, ApJ, 684, 1323
Pontoppidan, K. M., Dullemond, C. P., van Dishoeck, E. F., et al. 2005, ApJ, 622, 463
Pontoppidan, K. M., Fraser, H. J., Dartois, E., et al. 2003, A&A, 408, 981
Pontoppidan, K. M., Meijerink, R., Dullemond, C. P., & Blake, G. A. 2009, ApJ, 704, 1482
Pontoppidan, K. M., van Dishoeck, E., Blake, G. A., et al. 2011b, Msngr, 143, 32
Prantzos, N., Aubert, O., & Audouze, J. 1996, A&A, 309, 760
Ridge, N. A., Di Francesco, J., Kirk, H., et al. 2006, AJ, 131, 2921
Robitaille, T. P., Whitney, B. A., Indebetouw, R., Wood, K., & Denzmore, P. 2006, ApJS, 167, 256
Rosman, K. L. R., & Taylor, P. D. P. 1998, JPCRD, 27, 851
Rothman, L. S., Gordon, I. E., Barbe, A., et al. 2009, JQSRT, 110, 553
Scott, P. C., Asplund, M., Grevesse, N., & Sauval, A. J. 2006, A&A, 456, 675
Seifahrt, A., Käufl, H. U., Zängl, G., et al. 2010, Msngr, 142, 21
Sheffer, Y., Federman, S. R., Lambert, D. L., & Cardelli, J. A. 1992, ApJ, 397, 482
Sheffer, Y., Lambert, D. L., & Federman, S. R. 2002, ApJL, 574, L171
Shu, F. H. 1977, ApJ, 214, 488
Smith, R. L., Pontoppidan, K. M., Young, E. D., Morris, M. R., & van Dishoeck, E. F. 2009, ApJ, 701, 163
Tamayo, D., Triaud, A. H. M. J., Menou, K., & Rein, H. 2015, ApJ, 805, 100
Thi, W.-F., van Dishoeck, E. F., Pontoppidan, K. M., & Dartois, E. 2010, MNRAS, 406, 1409
Tielens, A. G. G. M., & Hagen, W. 1982, A&A, 114, 245
van Dishoeck, E. F., & Black, J. H. 1988, ApJ, 334, 771
van Dishoeck, E. F., Helmich, F. P., de Graauw, T., et al. 1996, A&A, 315, L349
van Kempen, T. A., van Dishoeck, E. F., Salter, D. M., et al. 2009, A&A, 498, 167
Visser, R., van Dishoeck, E. F., & Black, J. H. 2009, A&A, 503, 323
Vuong, M. H., Montmerle, T., Grosso, N., et al. 2003, A&A, 408, 581
Warin, S., Benayoun, J. J., & Viala, Y. P. 1996, A&A, 308, 535
Watanabe, N., & Kouchi, A. 2002, ApJL, 571, L173
Wilson, T. L. 1999, RPPh, 62, 143
Woods, P. M., & Willacy, K. 2009, ApJ, 693, 1360
Wouterloot, J. G. A., Henkel, C., Brand, J., & Davis, G. 2008, A&A, 487, 237
Young, E. D., Gounelle, M., Smith, R. L., Morris, M. R., & Pontoppidan, K. M. 2011, ApJ, 729, 43
Young, E. D., Kuramoto, K., Marcus, R. A., Yurimoto, H., & Jacobsen, Stein B. 2008, Reviews in Mineralogy & Geochemistry, Vol. 68, 187